る．SVMPには様々な分子量のものが存在するが，そのドメイン構造に基づき，P-IからP-IV型に分類されている（**図1**）[7]．P-I型は約200アミノ酸残基のメタロプロテアーゼ（M）ドメインのみから成るSVMPである．P-II型はMドメインに続きディスインテグリン（D）ドメインを有する遺伝子構造を持つが，タンパク質レベルでの存在が明確でないことから，主に翻訳後に切断を受けてディスインテグリンを生じる前駆体としての機能を担っていると考えられている．P-III型SVMPはMDドメインおよびそれに続く約100アミノ酸から成るシステイン残基に富むシステインリッチ（C）ドメインを持つ．Cドメインのアミノ酸配列は既知構造モチーフとの相同性が見られない．P-IV型はP-III型と同様のMDCドメインから成る長鎖とCLP様構造を持つ軽鎖2本から成るヘテロ三量体型のSVMPで，後で紹介するRVV-Xがその代表例である．これらSVMPのアミノ酸配列あるいはcDNA配列は1990年前後から相次いで決定されたが，これには岩永貞昭先生（現化血研顧問）らの研究グループ貢献が大きい．その後哺乳動物にもP-III型SVMPと類似のMDCドメイン構造を持つメタロプロテアーゼが見つかり，新規のメタロプロテアーゼファミリーとして注目された．ADAM(a disintegrin and metalloproteinase）はその構成ドメインやタンパク質の由来などに基づいて命名された[8]．adamalysin，reprolysinあるいはMDC proteinなどとも呼ばれるが，現在では特に哺乳動物由来のものについてはADAMが広く用いられている．ファーティリン（ADAM1，2）は受精時の膜融合に関わる精子表面タンパク質として，メルトリン（ADAM9，12および19）は筋管形成時の膜融合に関わる分子として報告された[9)10]．いずれも当初想定された膜融合への直接関与は示されていないが，その後tumor necrosis factor-α（TNF-α）の切断遊離酵素（TNF-α converting enzyme, TACE）が17番目のADAM分子として報告され[11)12]，ADAMの生体内での重要な役割が認識されるようになった．現在までに約40種のADAMが報告され，ヒトの生体内では20のADAM遺伝子が機能していることが分かっている[8]．哺乳動物ADAMの多くはMDCドメインの後にEGFドメインを介して一回膜貫通領域を持つI型膜タンパク質であるが，スプライスバリアントとしてSVMPの様に可溶性プロテアーゼとして機能するものも報告されている．ADAMは各種増殖因子やサイトカインの前駆体，その受容体やカドヘリンなどの細胞接着分子などの切断遊離（ectodomain shedding）に関与し，リウマチ等の炎症性疾患，アルツハイマー病やがんなど，様々な疾患に関与することが知られている[8]．1997年にADAMと相同性があるが，膜貫通領域を持たず，反復したトロンボスポンジン・タイプIモチーフ構造を有するメタロプロテアーゼが報告された[13]．同様のタンパク質はヒトでは19存在し，ADAMTS（ADAM with thrombospondin type1 motif）ファミリーと呼ばれている[14]．VWF切断酵素ADAMTS13は13番目に報告されたADAMTS分子である．

3. ADAMの基本立体構造

1993年にP-I型SVMPであるadamalysinIIの結晶構造が解明され[15]，その後複数のP-I型SMVPやヒトADAMのMドメインの結晶構造が報告されている[16)17]．Mドメインは亜鉛イオンに配位する3つのヒスチジン残基と活性基として機能するグルタミン酸残基を含むコンセンサス配列（HEXXHXXGXXHD）とその下流にMetターンと呼ばれる3つのヒスチジン残基を底部で支える保存されたメチオニン残基を持つ．Mドメインの詳細な構造が明らかになっている一方，P-III型SVMPあるいはADAMのMDCドメイン全体の立体構造は長らく不明であった．著者らは北米に生息するガラガラヘビ（*Crotalus atrox*）由来のP-III型SVMPであるVAP1（vascular apoptosis-inducing protein-1）およびVAP2のX線結晶構造解析を行い，哺乳動物ADAMと共通した立体構造をはじめて明らかにした（**図2A**）．詳細な構造は原著[18)19]あるいは総説等[20)-22]を参照して頂くとして，ここではエッセンスのみを紹介したい．P-III型SVMPとヒトADAMは分子全体で約40%程度のホモロジーを持つが，17あるSS結合や構造的なカルシウムイオン結合などMDCドメインの立体構造保持に関わるアミノ

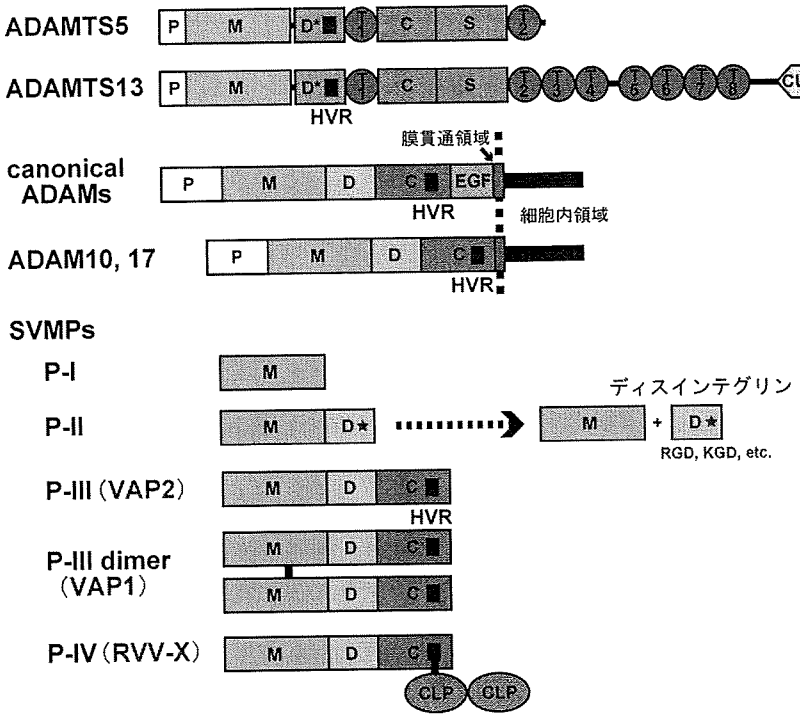

図1　SVMP，ADAMおよびADAMTSファミリープロテアーゼのドメイン構造の模式図．各ドメインを色分けして模式的に示す．

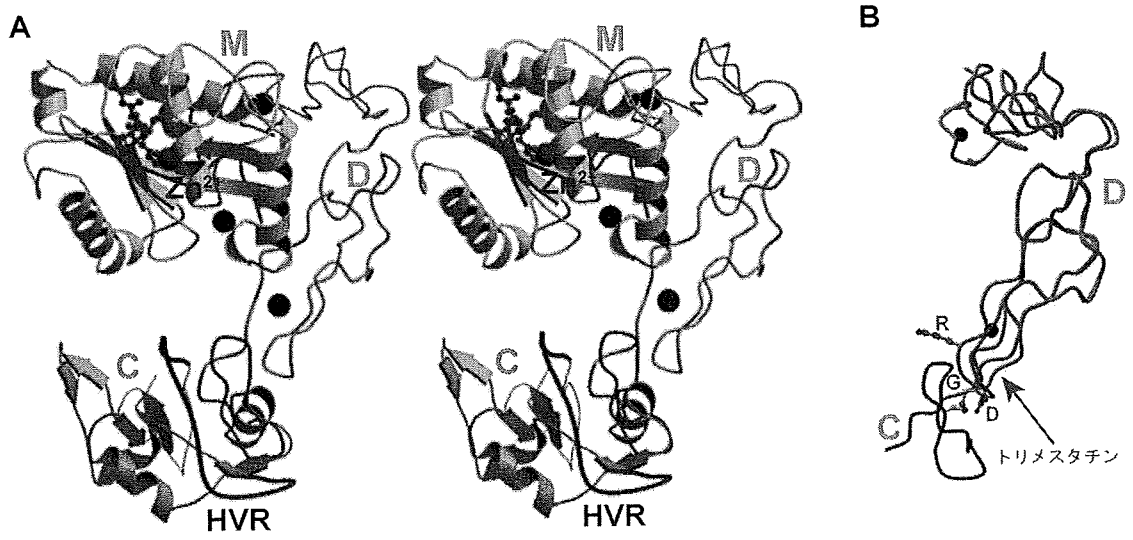

図2　ADAMのMDCドメイン部の立体構造．(A) VAP2の結晶構造（PDBID：2DW0）のステレオ図．亜鉛イオン，カルシウムイオンをそれぞれ赤，黒の球で示す．阻害剤GM6001をマゼンタ，HVRを青で示す．Mドメイン（黄），Dドメイン（シアン＋ピンク），Cドメイン（グレー＋黄緑）を示す．(B) VAP2のDドメイン（Aと同色で示す）とRGDディスインテグリン・トリメスタチン（黄緑色）の結晶構造の重ね合わせ．ADAMではディスインテグリンのRGD配列に相当する部分が続くCドメインとのインターフェースとして用いられ，SS結合を含む連続構造をなしている．

酸残基はほぼ全て保存されていることが明らかになった．MDCドメインは全体としてアルファベットのC字型の形状を持ち，両末端部が近接していた．Cドメインは新規のフォールディングを持つことが分かった．興味深いことにインテグリンに作用するディスインテグリンとADAMのDドメインは全体の形状は非常に良く似ているものの，RGD配列に相当する領域がADAMのDドメインでは続くCドメインとの境界に位置し，SS結合を含む連続した構造となっていた（**図2B**）．すなわちADAMあるいはP-III型SVMPはRGD配列を含むディスインテグリンと同様な機序でのインテグリン結合活性を持たないことが示唆された．一方でC字型の分子構造で触媒部位に対面するCドメイン内の領域が非常に興味深い性質を持つことが判明した．我々は超過変領域（hyper variable region：HVR）と名づけたが，SVMP間あるいはADAM間で最もアミノ酸配列の保存性が低く，長さも多様な領域である．HVRは分子構造的にも溶媒露出度が高く柔軟なループ構造を持ち，インデュースドフィットによるタンパク質間相互作用に適した構造を持つ．また，C字型のMDCドメイン構造の中で触媒部と対面する位置に存在する（**図2A**）．これらのことから著者らはHVRが基質そのもの，あるいは基質と相互作用するタンパク質と結合する部位である，即ち異なるADAMあるいはP-III型SVMPは異なるHVRを持ち異なるターゲットを認識する，という作業仮説を提案した[18) 20)]．

P-III型SVMPの多くはP-I型に比べて高い出血活性を持つが，多くの場合実際のターゲット分子が不明で，またその作用メカニズムも良く分かっていない．一方，膜型ADAMについても基質の切断部位にコンセンサス配列が無く，どのように基質を識別しているかが不明である．構造的知見を基に，今後基質の同定や作用機序の解明が進むことを期待したい．

4. ADAMTSプロテアーゼの部分立体構造

当初ADAMTSファミリーに属するプロテアーゼはADAMと同様にMおよびDドメインを持ち，そのC末端側に最初のTSR（T1）ドメインが挿入され，Cドメインが続くと考えられていた（**図1**）．しかし，最近ADAMTS 1，4および5の部分結晶構造が解明され，これまでDドメインとされていた領域（今後D*と呼ぶ）がディスインテグリン様の立体構造を持たず，実はADAMのCドメインと相同の構造を持つことが明らかになった[23) 24)]．そのADAMTSのD*ドメインの立体配置であるが，Mドメイン部分でADAMと重ね合わせると非常に興味深い（**図3A**）．先に述べたようにADAMのCドメインはC字型のMDCドメイン構造により切断基質の上流側で（図では左側より）触媒部と対面する．しかし，ADAMTSではMドメインのC末端側はADAMと反対側に伸びたループ構造であり，続くD*ドメインはMドメインと直接接触し，基質切断部位の下流側（図で右側）に位置している．即ち，ADAMとADAMTSではMドメインに対するC末端側のドメインの相対的位置が全く異なる．さらに興味深いことにD*ドメインのHVRはMドメインの基質が結合する溝からそのまま続く領域に位置し，切断基質のC末端側領域を直接認識する可能性が強く示唆されている（**図3B**）[20)]．最近，ADAMTS13のD*ドメインHVR内のアミノ酸残基がVWFの切断に重要であることが示され，HVRが基質認識に直接関与することがはじめて実験的に示された[25)]．

5. ラッセルクサリヘビ毒X因子活性化酵素

インド，東南アジア地区に広く生息するラッセルクサリヘビ（*Daboia russelli russelli* および *Daboia russelli siamensis*）の毒は古くより非常に強い血栓形成作用を持つことが知られている．この蛇毒にはX因子およびIX因子に特異的に作用して活性化する酵素RVV-X（Russell's viper venom factor X activator）が含まれ，その基質特異性の厳密さから注目されてきた[26)]．RVV-XによるX因子の水解には生理的な活性化とは異なりリン脂質膜や他のタンパク質との複合体形成が必要ない．また触媒部の立体構造が全く異なるため，血液中に存在するセリンプロテアーゼインヒビター（セルピン）が作用しない点が特徴である．先に述べたようにRVV-XはP-IV型SVMP

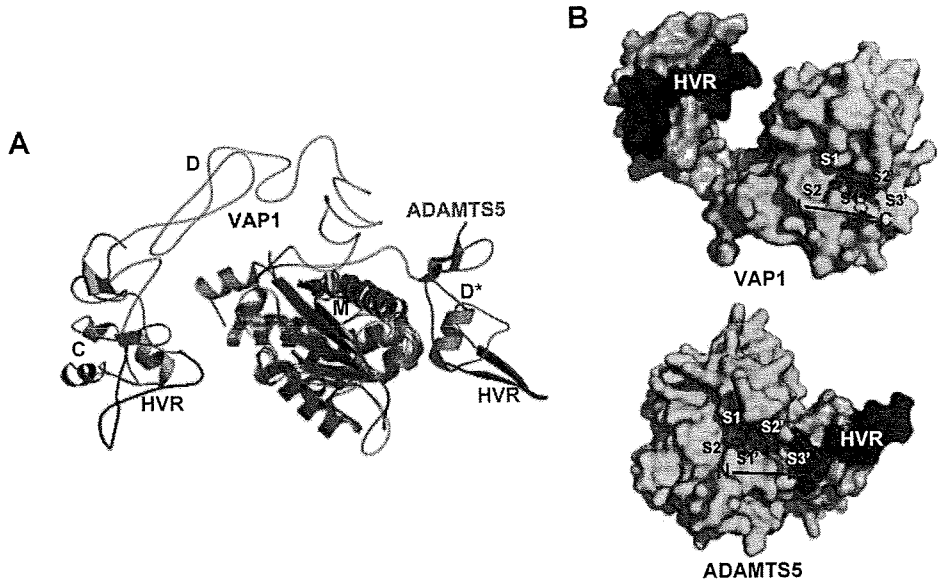

図3　ADAM（VAP1）とADAMTS（ADAMTS5）の構造比較．（**A**）VAP1（PDBID:2ERP）とADAMTS5（PDBID:2RJQ）のMドメインの重ね合わせを示す．Mドメインの構造は非常に保存されているが，続くC末側ドメインの位置関係はVAP1とADAMTS5で大きく異なる．（**B**）VAP1（左）およびADAMTS5（右）の触媒部位とHVRの関係をそれぞれ分子表面モデルで示す．Mドメインを黄色，C（D*）ドメインを黄緑色，HVRを青色，その他の部分をグレーで示す．それぞれ，阻害剤（マゼンタ）の結合様式から基質の認識様式（結合部位S2-S2'）が推測されている．

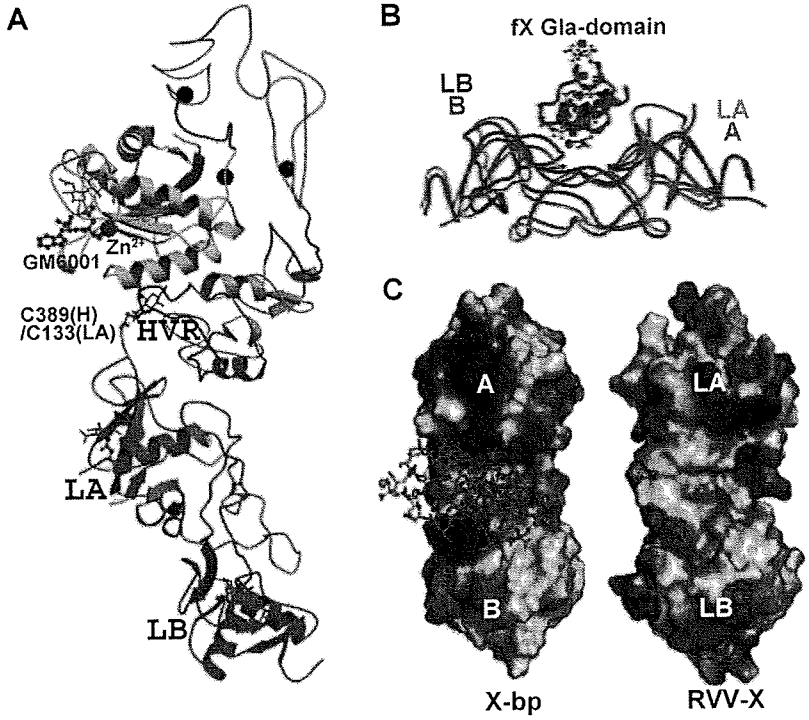

図4　RVV-Xの結晶構造．（**A**）重鎖の各サブドメインは図2に準じた色で，軽鎖はオレンジ（LA）及びマゼンタ（LB）で示す．結合する亜鉛イオン（赤），カルシウムイオン（黒）は球で示す．（**B**）X-bp/GLAドメイン複合体（PDBID：1IOD，CLP部分をグレー，GLAドメインをピンク，結合したカルシウムイオンを緑色で示す）とRVV-X軽鎖部（オレンジおよびマゼンタ）の重ね合わせ．（**C**）X-BP（左）とRVV-X軽鎖部（右）の表面形状および電荷分布の比較．

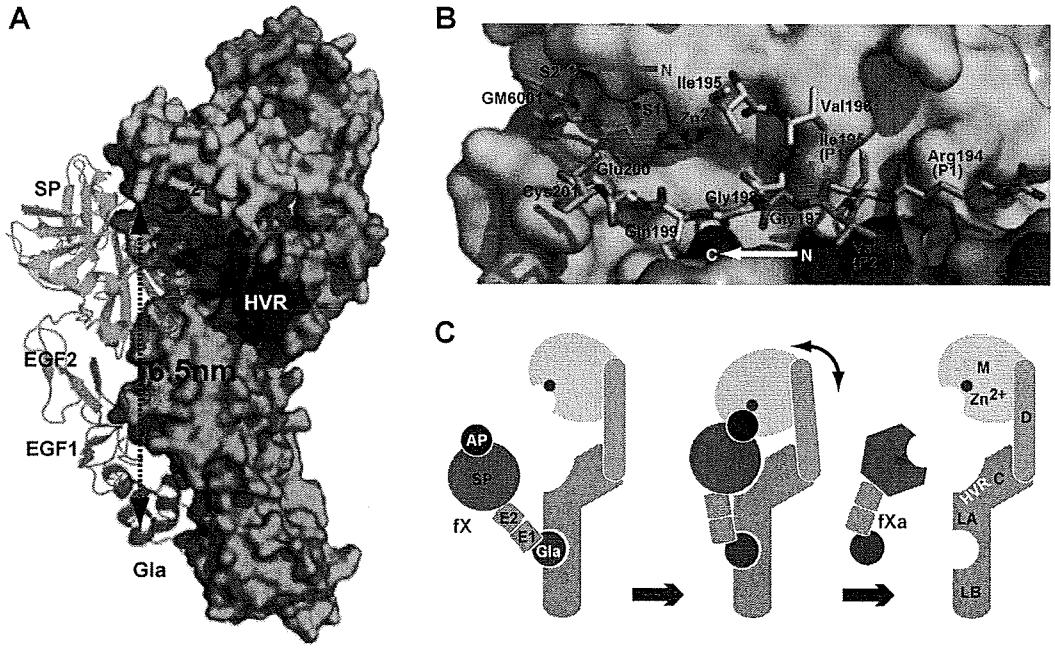

図5 RVV-XによるX因子活性化機構．(**A**) ドッキングモデル．RVV-Xは図4に準じて色付けした分子表面を示し，Xa因子はリボンモデルで示す．Xa因子はセリンプロテアーゼ（SP），EGFドメインを鎌田らの結晶構造（PDBID：1XKA），GLAドメインを水野らの結晶構造（PDBID:1IOD）を基にドメインの可動性を考慮してモデルを作成した．(**B**) X因子側より見たドッキングモデルを示す．活性化したXa因子（グレー）では切断端のIle195のアミノ基は分子内部に潜り込んでいるが，前駆体の活性化ペプチド（AP）はピンクで示すように分子表面に露出した構造を持つと推測される．この時切断されるペプチド鎖の向きは阻害剤GM6001（緑色）の結合様式から推測される基質の触媒部位への結合の向きと一致する．(**C**) RVV-XによるX因子活性化機構の模式図．

であり，分子内にADAM型の長鎖とCLP型の軽鎖2本を含むヘテロ三量体であり，軽鎖同士および一つの軽鎖と長鎖はSS結合で結ばれている．このラッセルクサリヘビ毒にはRVV-Xとは別にV因子に作用し活性化する酵素RVV-Vの存在が知られるが，こちらはトロンビン様のセリンプロテアーゼである．

6. RVV-Xの立体構造

著者らはRVV-Xの結晶構造を2.9 Åの分解能で決定した（**図4**）[27]．アミノ酸配列からの予想通り，分子はP-III型SVMPやADAMのC字型のMDCドメイン構造を持つ長鎖部とCLP構造を持つ軽鎖（LAおよびLB）から成っていた（**図4A**）．長鎖のHVR領域にあるシステイン残基C389とLAのC末端システイン残基（C133）間のSS結合が確認された．また，HVRとLAはSS結合のみならず，複数の疎水性残基同士の相互作用を形成し，その結果長鎖のCドメインと軽鎖部は一体として機能することが示唆された．軽鎖部は凝固因子結合タンパク質群（X-bp，IX-bpおよびIX/X-bp[3) 28)]と表面電荷分布を含め，非常に類似した構造を持つ（**図4B, C**）．X-bpはX因子のGlaドメインに非常に高い親和性で結合し無力化する毒素である．構造の類似性からRVV-Xが2本の軽鎖の中央部で形成する窪みがGlaドメインを認識するエクソサイトである可能性が示唆された．HVR内のシステイン残基C389は他のSVMPやADAMには見られず，またLAのC133はX-bpなど凝固因子Glaドメインに結合する蛇毒CLPでは保存されていない．血小板GPI bに作用するフラボセチンAのαサブユニットはRVV-XのLAと同じ箇所にシステイン残基を有している．フラボセチンAではもう一方のβサブユニットがN末端に余分なシステイン残

基を有し，これらが互い違いにSS結合を成して環状4量体構造を形成している[29]．

7. RVV-XによるX因子活性化機構

得られたRVV-Xの結晶構造と既に報告されているXa因子（PDB：1XKA）[30)31)]およびX-bpとX因子Glaドメイン複合体の結晶構造[28)32)]（PDB：1IOD）を基にドッキングモデルを作成した[27]．これまでの知見からX因子の二つのEGFドメイン間およびGlaドメインとFGF1の間は溶液中で高い自由度を持つことが示されている．Glaドメインが X-bpと同様にRVV-X軽鎖の中央部に結合すると仮定すると，想定されるドメイン間の可動範囲でRVV-X分子の表面に分子構造の凹凸を基にXa因子の分子構造をうまく合わせることが出来た（**図5**）．前駆体であるX因子の結晶解析はなされていないが，他のセリンプロテアーゼ同様に前駆体では切断部位（Arg194-Ile195結合）が分子表面に露出していると考えられる（**図5B**）．このドッキングモデルでは想定される切断部のポリペプチド鎖の向きがちょうどRVV-Xの活性クレフトに結合できる向きと一致し，またMDC部に内在する可動性で十分結合可能な近傍に位置している．

RVV-Xは触媒部と立体構造的に約6.5nm離れて存在するエクソサイトでX因子のGlaドメインを認識することで高い基質特異性を発揮すると考えられる（**図5C**）．このモデルはRVV-XがGlaドメインを欠損したX因子を活性化出来ない事，また活性化にGlaドメインのフォールディングに必要なmMオーダーのカルシウムイオンの存在が必要な事など[26]，これまでの知見をよく説明する．

8. おわりに

著者らはADAMにおいてHVRが基質あるいは基質と結合するタンパク質を認識する部位であるとの仮説を提案した．RVV-XはX因子のGlaドメインを認識するエクソサイト部を軽鎖として持ち，HVRはその軽鎖とのインターフェースとして機能している点で大変興味深い．RVV-X軽鎖はX-bp等と同様にドメインスワッピング[1)3)]によりGlaドメイン結合性を獲得したと考えられるが，さらにMDCドメイン構造を有するメタロプロテアーゼのHVR部と結合することで，RVV-Xは基質特異性の非常に高い酵素として進化したと考えられる．RVV-Xの立体構造とそれから見出される作用規序は，蛇毒素と生体分子の相互作用の理解に留まらず，ADAMおよびADAMTSプロテアーゼの基質認識機構にも重要な示唆を与えるものである．

文　献

1) 山崎泰男，森田隆司：毒ヘビによってつくりだされる血液毒蛋白質の構造と機能～トキシン研究はいまなお有効か？．蛋白質・核酸・酵素 **54**, 628-634, 2009.
2) 千谷晃一，松井太衛：蛇毒と血栓止血学．血栓止血誌 **16**, 233-235, 2005.
3) 森田隆司，水野洋：Factor IX/Factor X-binding proteinの立体構造と機能－3Dドメインスワッピング機構で新しい機能を獲得した血液凝固因子結合タンパク質－．血栓止血誌 **10**, 305-309, 1999.
4) 武谷浩之：ディスインテグリンの構造・機能相関．血栓止血誌 **11**, 211-217, 2000.
5) 松井太衛，広津晶子，水野洋：フォン・ビルブランド因子のモジュレータータンパク質であるボトロセチンの立体構造と機能．血栓止血誌 **12**, 240-245, 2001.
6) 井上克枝：Snakes know everything about human hemostasis. 血栓止血誌 **19**, 826-832, 2008.
7) Fox JW, Serrano SM：Structural considerations of the snake venom metalloproteinases, key members of the M12 reprolysin family of metalloproteinases. Toxicon **45**, 969-985, 2005.
8) Edwards DR, Handsley MM, Pennington CJ：The ADAM metalloproteinases. Mol Aspects Med **29**, 258-289, 2009.
9) Blobel CP, Wolfsberg TG, Turck CW, Myles DG, Primakoff P, White JM：A potential fusion peptide and an integrin ligand domain in a protein active in sperm-egg fusion. Nature **356**, 248-252, 1992.
10) Yagami-Hiromasa T, Sato T, Kurisaki T, Kamijo K, Nabeshima Y, Fujisawa-Sehara A：A metalloprotease-disintegrin participating in myoblast fusion. Nature **377**, 652-656, 1995.
11) Black RA, Rauch CT, Kozlosky CJ, Peschon JJ, Slack JL, Wolfson MF, Castner BJ, Stocking KL, Reddy P, Srinivasan S, Nelson N, Boiani N, Schooley KA, Gerhart M, Davis R, Fitzner JN, Johnson RS, Paxton RJ, March CJ, Cerretti DP：A metalloproteinase disintegrin that releases tumour-necrosis factor-alpha from cells. Nature **385**, 729-733, 1997.
12) Moss ML, Jin SL, Milla ME, Bickett DM, Burkhart W, Carter HL, Chen WJ, Clay WC, Didsbury JR, Hassler D, Hoffman CR, Kost TA, Lambert MH, Leesnitzer MA, McCauley P, McGeehan G, Mitchell J, Moyer M, Pahel G, Rocque W, Overton LK, Schoenen F, Seaton T, Su JL, Warner J, Willard D, Becherer JD：Cloning of a disintegrin metalloproteinase that processes precursor tumour-necrosis factor-alpha. Nature **385**, 733-736, 1997.
13) Kuno K, Kanada N, Nakashima E, Fujiki F, Ichimura F, Matsushima K：Molecular cloning of a gene encoding a new type of metalloproteinase-disintegrin family protein with thrombospondin motifs as an inflammation associated gene. J Biol Chem **272**, 556-562, 1997.

14) Porter S, Clark IM, Kevorkian L, Edwards DR : The ADAMTS metalloproteinases. Biochem J **386**, 15-27, 2005.
15) Gomis-Ruth FX, Kress LF, Bode W : First structure of a snake venom metalloproteinase : a prototype for matrix metalloproteinases/collagenases. EMBO J **12**, 4151-4157, 1993.
16) Maskos K, Fernandez-Catalan C, Huber R, Bourenkov GP, Bartunik H, Ellestad GA, Reddy P, Wolfson MF, Rauch CT, Castner BJ, Davis R, Clarke HR, Petersen M, Fitzner JN, Cerretti DP, March CJ, Paxton RJ, Black RA, Bode W : Crystal structure of the catalytic domain of human tumor necrosis factor-alpha-converting enzyme. Proc Natl Acad Sci U S A **95**, 3408-3412, 1998.
17) Orth P, Reichert P, Wang W, Prosise WW, Yarosh-Tomaine T, Hammond G, Ingram RN, Xiao L, Mirza UA, Zou J, Strickland C, Taremi SS, Le HV, Madison V : Crystal structure of the catalytic domain of human ADAM33. J Mol Biol **335**, 129-137, 2004.
18) Takeda S, Igarashi T, Mori H, Araki S : Crystal structures of VAP1 reveal ADAMs' MDC domain architecture and its unique C-shaped scaffold. EMBO J **25**, 2388-2396, 2006.
19) Igarashi T, Araki S, Mori H, Takeda S : Crystal structures of catrocollastatin/VAP2B reveal a dynamic, modular architecture of ADAM/adamalysin/reprolysin family proteins. FEBS Lett **581**, 2416-2422, 2007.
20) Takeda S : Three-dimensional domain architecture of the ADAM family proteinases. Semin Cell Dev Biol, **20**, 146-152, 2009.
21) Takeda S : VAP1 : snake venom homolog of mammalian ADAMs. in Handbook of Metalloproteins (ed. Messerschmidt, A.) John Wiley & Sons, Inc., 2008.
22) 武田壮一：ADAM ファミリータンパク質のドメイン構造．生化学 **79**, 1051-1055, 2007.
23) Gerhardt S, Hassall G, Hawtin P, McCall E, Flavell L, Minshull C, Hargreaves D, Ting A, Pauptit RA, Parker AE, Abbott WM : Crystal structures of human ADAMTS-1 reveal a conserved catalytic domain and a disintegrin-like domain with a fold homologous to cysteine-rich domains. J Mol Biol **373**, 891-902, 2007.
24) Mosyak L, Georgiadis K, Shane T, Svenson K, Hebert T, McDonagh T, Mackie S, Olland S, Lin L, Zhong X, Kriz R, Reifenberg EL, Collins-Racie LA, Corcoran C, Freeman B, Zollner R, Marvell T, Vera M, Sum PE, Lavallie ER, Stahl M, Somers W : Crystal structures of the two major aggrecan degrading enzymes, ADAMTS4 and ADAMTS5. Protein Sci **17**, 16-21, 2008.
25) de Groot R, Bardhan A, Ramroop N, Lane DA, Crawley JT : Essential role of the disintegrin-like domain in ADAMTS13 function. Blood, 2009.
26) Morita T : Proteases which activate factor X, 179-208 (Alaken, Colorado, 1998.
27) Takeda S, Igarashi T, Mori H : Crystal structure of RVV-X : An example of evolutionary gain of specificity by ADAM proteinases. FEBS Lett **581**, 5859-5864, 2007.
28) Mizuno H, Fujimoto Z, Atoda H, Morita T : Crystal structure of an anticoagulant protein in complex with the Gla domain of factor X. Proc Natl Acad Sci U S A **98**, 7230-7234, 2001.
29) Fukuda K, Mizuno H, Atoda H, Morita T : Crystal structure of flavocetin-A, a platelet glycoprotein Ib-binding protein, reveals a novel cyclic tetramer of C-type lectin-like heterodimers. Biochemistry **39**, 1915-1923, 2000.
30) Kamata K, Kawamoto H, Honma T, Iwama T, Kim SH : Structural basis for chemical inhibition of human blood coagulation factor Xa. Proc Natl Acad Sci U S A **95**, 6630-6635, 1998.
31) 鎌田健司，宮田敏行：凝固第 Xa 因子の立体構造．血栓止血誌 **10**, 181-188, 1999.
32) 森田隆司，水野洋：Gla ドメインの立体構造と機能．血栓止血誌 **11**, 391-396, 2000.

19. N. Knowles, M. D. Dettinger, D. R. Cayan, *J. Clim.* **19**, 4545 (2006).
20. P. W. Mote, A. F. Hamlet, M. P. Clark, D. P. Lettenmaier, *Bull. Am. Meteorol. Soc.* **86**, 39 (2005).
21. I. T. Stewart, D. R. Cayan, M. D. Dettinger, *J. Clim.* **18**, 1136 (2005).
22. A. L. Westerling, H. G. Hidalgo, D. R. Cayan, T. W. Swetnam, *Science* **313**, 940 (2006); published online 5 July 2006 (10.1126/science.1128834).
23. N. McDowell *et al.*, *New Phytol.* **178**, 719 (2008).
24. C. Bigler, D. G. Gavin, C. Gunning, T. T. Veblen, *Oikos* **116**, 1983 (2007).
25. A. W. Fellows, M. L. Goulden, *Geophys. Res. Lett.* **35**, L12404 (2008).

26. We thank the many people involved in establishing and maintaining the permanent forest plots; C. Allen, A. Das, J. Halofsky, J. Hicke, J. Lutz, and four anonymous reviewers for helpful comments on the manuscript; and J. Yee for essential statistical advice. The forest plots were funded by NSF's Long-term Studies Program (DEB-0218088); the Wind River Canopy Crane Program through cooperative agreement PNW 08-DG-11261952-488 with the USDA Forest Service Pacific Northwest Research Station; various awards through the USDA Forest Service's Pacific Northwest, Pacific Southwest, and Rocky Mountain research stations and the McIntire-Stennis Cooperative Forestry Program; NSF awards DEB-0743498 and BCS-0825823; the Natural Science and Engineering Research Council of Canada; and various awards through the U.S. National Park Service and U.S. Geological Survey (USGS). This work is a contribution of the Western Mountain Initiative (a USGS global change research project) and the Cordillera Forest Dynamics Network (CORFOR).

Supporting Online Material

www.sciencemag.org/cgi/content/full/323/5913/521/DC1
Materials and Methods
SOM Text
Figs. S1 to S6
Tables S1 to S4
References

22 August 2008; accepted 3 December 2008
10.1126/science.1165000

The Sphingolipid Transporter Spns2 Functions in Migration of Zebrafish Myocardial Precursors

Atsuo Kawahara,[1,2]* Tsuyoshi Nishi,[3,4] Yu Hisano,[3,4] Hajime Fukui,[1] Akihito Yamaguchi,[3,4] Naoki Mochizuki[1]

Sphingosine-1-phosphate (S1P) is a secreted lipid mediator that functions in vascular development; however, it remains unclear how S1P secretion is regulated during embryogenesis. We identified a zebrafish mutant, *ko157*, that displays cardia bifida (two hearts) resembling that in the *S1P receptor-2* mutant. A migration defect of myocardial precursors in the *ko157* mutant is due to a mutation in a multipass transmembrane protein, Spns2, and can be rescued by S1P injection. We show that the export of S1P from cells requires Spns2. *spns2* is expressed in the extraembryonic tissue yolk syncytial layer (YSL), and the introduction of *spns2* mRNA in the YSL restored the cardiac defect in the *ko157* mutant. Thus, Spns2 in the YSL functions as a S1P transporter in S1P secretion, thereby regulating myocardial precursor migration.

During the late stages of zebrafish segmentation characterized by the formation of the somites, the myocardial precursors from both sides of the anterior lateral plate mesoderm migrate toward the midline to form the heart tube (*1*, *2*). Forward genetic analysis in zebrafish has helped to uncover genes involved in vertebrate heart formation (*3*). To identify additional regulators of heart development, we performed *N*-ethyl-*N*-nitrosourea (ENU) mutagenesis screening for mutations specifically affecting cardiac morphogenesis. We isolated a recessive *ko157* mutant that displayed two hearts, a condition known as cardia bifida with swollen pericardial sacs (Fig. 1, A, B, E, and F). The expression of myocardial markers [*nkx2.5* and *cardiac myosin light chain 2* (*cmlc2*)] and chamber-specific markers [*atrial myosin heavy chain* (*amhc*) and *ventricular myosin heavy chain* (*vmhc*)] was detected in two separated domains (Fig. 1, C and G, and fig. S2); this finding suggests that the myocardial precursors failed to migrate but differentiated into two chambers at the bilateral positions.

The migration of several mesodermal derivatives examined by the expression pattern of a vascular marker (*fli1*), an erythroid marker (*gata1*), a pronephric marker (*pax2*), and a lateral plate mesoderm marker (*hand2*) was not impaired in *ko157* mutants (figs. S2 and S3), which suggests that the migration of myocardial precursors is dominantly affected. Besides cardia bifida, there were abnormal blisters at the tip of the tail in the mutant (Fig. 1, D and H). These two characteristic phenotypes (cardia bifida and tail blisters) in the *ko157* mutant were similar to those in the *miles apart* (*mil*)/*S1P receptor-2* (*S1P2*) mutant (*4*). Sphingosine-1-phosphate (S1P) is a lipid mediator involved in cell growth, death, migration, and differentiation (*5*–*8*). Both cardia bifida and tail blisters were observed in embryos injected with an antisense morpholino for *mil*/*S1P2* (*mil* MO; 15 ng) (*9*) (fig. S4 and table S1), suggesting a genetic interaction between *ko157* and *mil*/*S1P2*.

Genetic mapping of the *ko157* mutation by means of simple sequence length polymorphism

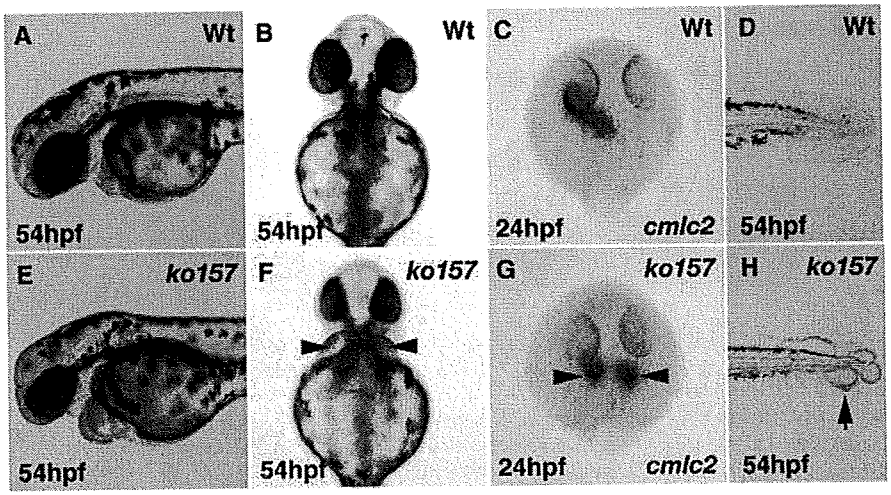

Fig. 1. Morphological phenotypes of *ko157* mutants. (**A**, **B**, **D**, **E**, **F**, and **H**) Stereomicroscopic views of wild-type (Wt) embryo [(A), (B), and (D)] and *ko157* mutant [(E), (F), and (H)]. Two swollen pericardial sacs (arrowheads) at 54 hours post-fertilization (hpf) were observed in *ko157* mutant [(E) and (F)] but not in Wt embryos [(A) and (B)]. (B) and (F) are ventral views. (**C** and **G**) Two hearts (arrowheads) in *ko157* mutants at 24 hpf were visualized (dorsal view) by whole-mount in situ hybridization with antisense *cmlc2* probe. *ko157* mutant (H), but not Wt embryos (D), exhibited tail blisters (arrow).

[1]Department of Structural Analysis, National Cardiovascular Center Research Institute, Fujishirodai 5-7-1, Suita, Osaka 565-8565, Japan. [2]HMRO, Kyoto University Faculty of Medicine, Yoshida, Sakyo-Ku, Kyoto 606-8501, Japan. [3]Department of Cell Membrane Biology, Institute of Scientific and Industrial Research, Osaka University, 8-1 Mihogaoka, Ibaraki-shi, Osaka 567-0047, Japan. [4]Graduate School of Pharmaceutical Sciences, Osaka University, Suita-shi, Osaka 565-0871, Japan.

*To whom correspondence should be addressed. E-mail: atsuo@ri.ncvc.go.jp

(SSLP) markers revealed that the locus of *ko157* was very close to z9419 and z63525 on linkage group 5 (Fig. 2A). We found that the *ko157* mutant allele contained a point mutation in the *spns2* gene with a substitution of arginine to serine at amino acid position 153 (R153S). This arginine is conserved between zebrafish Spns2 and mammalian homologs of Spns2 (fig. S5). Spns1 is a member of the Spns protein family (*10*, *11*), but injection of *spns1* MO (8 ng) into wild-type embryos did not induce cardia bifida, and injection into *ko157* embryos did not worsen the phenotype (fig. S6). Hence, Spns2, but not Spns1, is involved in cardiac morphogenesis.

To examine whether the mutation in Spns2 caused the functional impairment in *ko157* mutants, we performed knockdown analysis with antisense morpholino (*spns2* MO). The *spns2* MO injection, but not control morpholino, (5-base mismatched control morpholino for *spns2* MO; 5-mis MO), suppressed the production of the mature form of *spns2* mRNA (fig. S7). Injection of *spns2* MO resulted in cardia bifida (table S1; 86%, n = 69) with bilateral expression of *cmlc2* (Fig. 2, B to D), with no cardia bifida in control 5-mis MO–injected embryos (table S1; 0%, n = 68). To evaluate whether *spns2* could rescue the *ko157* mutant phenotype, we injected *spns2* or *spns2(R153S)* (*spns2* mutant) mRNA (250 pg) into the embryos derived from *spns2*^{ko157} heterozygous carriers. Using more than 250 pg caused severe defects in the trunk and the tail as well as observation of one beating heart (fig. S8). Injection of *spns2* mRNA, but not mutant *spns2(R153S)* mRNA, effectively restored both the migration of myocardial precursors and the tail blisters (Fig. 2, E to G, fig. S9, and table S2). Injection of human *Spns2* (*hSpns2*) mRNA also rescued the cardia bifida phenotype in the *spns2*^{ko157} mutant, whereas injection of the corresponding *hSpns2* mutant, *hSpns2(R199S)*, did not (fig. S10 and table S3). The *spns2*^{ko157} mutant phenotype was not restored by injection of a construct in which human Spns1 is fused to enhanced green fluorescent protein (EGFP), *hSpns1-EGFP* (fig. S10 and table S3). These results show that Spns2 function is conserved from fish to mammals and that Spns1 cannot compensate for the loss of Spns2.

Because the cardia bifida phenotype in the *spns2*^{ko157} mutant was similar to that in the *mil/S1P2* mutant, we investigated a possible genetic interaction between *spns2* and *mil/S1P2*. Injection of *mil* MO induced cardia bifida in embryos derived from a wild-type–*Tg(cmlc2:mRFP)* cross in a dose-dependent manner (table S1, *mil* MO 15-ng injection; 90%, n = 49; table S4, *mil* MO

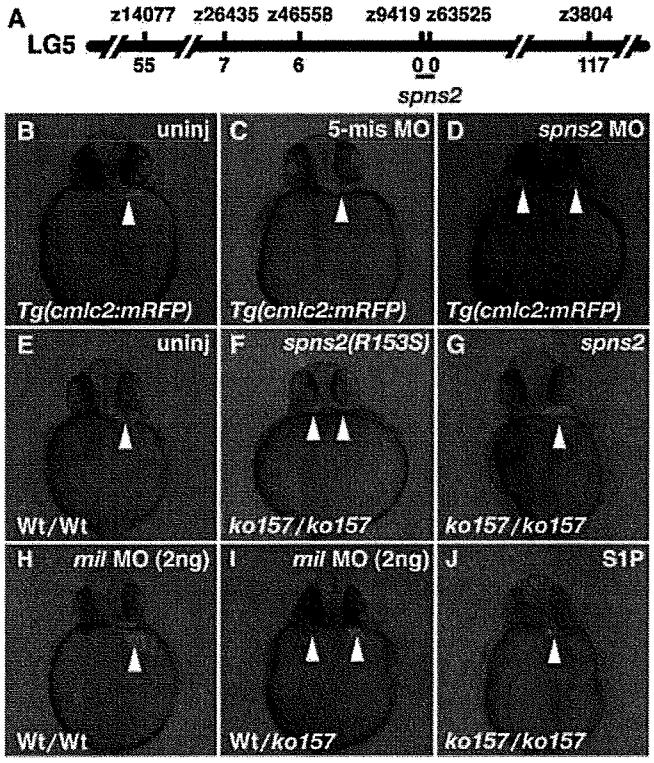

Fig. 2. The gene responsible for the *ko157* mutant encodes *spns2* and is associated with S1P signaling. (**A**) Genetic map of the *ko157* on linkage group 5 (LG5). The numbers of recombination events between SSLP markers and the *ko157* locus in 400 *ko157* mutant embryos (400 diploid) are shown. (**B** to **D**) Injection of *spns2* MO (10 ng) but not 5-mis MO (10 ng) led to cardia bifida, as determined by mRFP expression (*cmlc2* expression domain) (arrowheads). (**E** to **G**) Cardia bifida in *ko157* was recovered by injection of *spns2* mRNA (250 pg) but not *spns2 (R153S)* mRNA (250 pg) at the one-cell stage. (**H** and **I**) Cardia bifida was observed when *mil* MO (2 ng) was injected into heterozygous (Wt/*ko157*) but not Wt (Wt/Wt) embryos. (**J**) Cardia bifida in *ko157* was restored by S1P (1 ng) injection in deep area of the blastomeres at blastula stage. Genotypes were confirmed by direct sequencing of the *ko157* locus [(E) to (J)]. All views are ventral at 28 hpf.

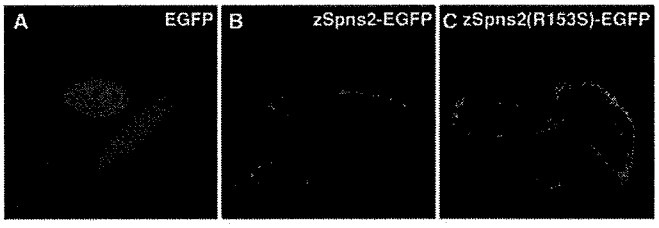

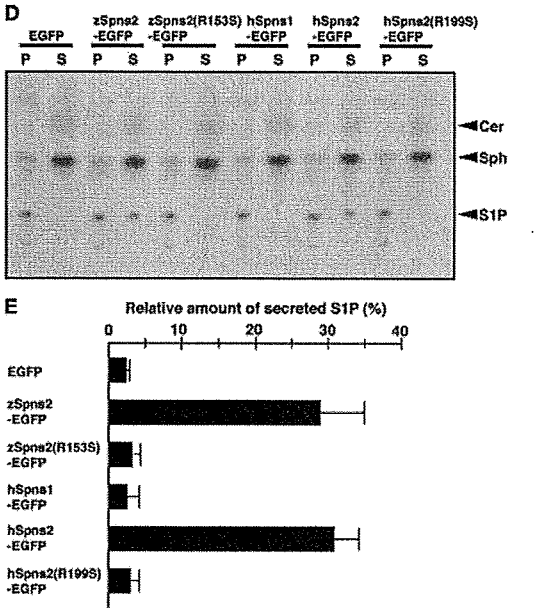

Fig. 3. Plasma membrane–localized Spns2 exports S1P from the cells. (**A** to **C**) Confocal fluorescence microscopy images of CHO cells expressing mouse SphK1 transfected with the plasmids indicated. (**D**) [^{3}H]S1P converted from [^{3}H]sphingosine in the lipids extracted from medium (S, supernatant) and cells (P, pellet) was separated on a thin-layer chromatography plate. Cer, Sph, and S1P indicate the positions of [^{3}H]ceramide, [^{3}H]sphingosine, and [^{3}H]S1P, respectively. (**E**) Relative amount of secreted S1P indicates the percentage of total [^{3}H]S1P (P + S). Data are expressed as means ± SD of more than three independent experiments of (D).

2-ng injection; 7%, $n = 55$). Low-dose *mil* MO (2 ng) injections in *spns2*^{ko157} heterozygous embryos resulted in a higher frequency of cardia bifida relative to wild-type embryos (table S4; 44%, $n = 18$). Genotyping revealed that most cardia bifida embryos were wild-type/*ko157* (Fig. 2, H and I, and table S4). The severity of the cardiac defect was comparable between *mil* MO (15 ng)–injected wild-type and *mil* MO–injected *ko157* embryos (fig. S11). These data suggest that *spns2* genetically interacts with *mil/S1P2*.

To further examine the functional interaction of Spns2 and S1P signaling, we performed a rescue experiment of the *spns2*^{ko157} mutant by S1P injection. When S1P (1 ng) was injected deep into an area of the blastomeres of blastula-stage embryos derived from *spns2*^{ko157} heterozygous carriers, cardia bifida was effectively restored (Fig. 2J and table S2). In addition, the cardia bifida phenotype induced by *mil* MO (15 ng) injection into the yolk was not rescued by subsequent injection of *spns2* mRNA (250 pg) into the blastomere of one- to two-cell–stage embryos (fig. S12), which suggests that Spns2 functions upstream of Mil/S1P$_2$ (fig. S1).

The putative 12-transmembrane domains, together with the predicted structural similarity between zebrafish Spns2 (zSpns2) and the bacterial glycerol-3-phosphate transporter (*12*) and the genetic interaction of Spns2 and the S1P-mediated signaling, suggested that Spns2 might function as a S1P transporter. To test this, we used Chinese hamster ovary (CHO) cells expressing a sphingosine kinase, *mSphK1*, essential for S1P synthesis (CHO-SphK cells) (fig. S1). Although [^{3}H]sphingosine was taken up by the cells and effectively converted to [^{3}H]S1P, it was not secreted because of the absence of an S1P export activity. We examined whether the expression of zSpns2-EGFP or zSpns2(R153S)-EGFP was able to induce S1P export. Both zSpns2-EGFP and zSpns2(R153S)-EGFP were predominantly localized within the plasma membrane and in the endosomes of transfected CHO-SphK cells (Fig. 3, A to C), consistent with a role in membrane trafficking. Expression of zSpns2-EGFP resulted in a time-dependent export of [^{3}H]S1P that was not seen in either the EGFP- or zSpns2(R153S)-EGFP–transfected cells (Fig. 3, D and E, and fig. S13). Moreover, endogenous S1P release was also detected only in the medium from the zSpns2-EGFP–expressing cells (fig. S14) without altering the content of cellular sphingolipids (fig. S15). Overexpression of hSpns2-EGFP enhanced S1P export to a similar extent as zSpns2-EGFP, whereas that of hSpns2(R199S)-EGFP and hSpns1-EGFP did not (Fig. 3, D and E). S1P release was not due to cell death induced by Spns2-EGFP expression (fig. S16), and the activity of sphingosine kinase in the medium was not affected by Spns2-EGFP expression (fig. S17).

Recently it was proposed that ABC transporters including ABCC1 and ABCA1 are required for S1P transport (*13*–*15*). The cellular distribution of Spns2-EGFP is similar to that of ABCA1 (*16*). Therefore, the net S1P release to the outside of the cells would depend on the amount of Spns2 and other S1P transporters expressed on the plasma membrane. The contribution of ABC transporters in the S1P transport is still controversial in vivo because the quantity of plasma S1P is not altered in mice deficient for ABCC1 or ABCA1 (*17*). We propose that Spns2 is a S1P transporter essential for the S1P-mediated signaling pathway in vivo (fig. S1).

To further understand where and how Spns2 functions in vivo, we examined *spns2* expression during early embryogenesis by whole-mount in situ hybridization. The expression of *spns2* was induced at the marginal cells of the blastoderm at dome stage (fig. S18). During gastrulation stages, *spns2* was predominantly expressed in the extraembryonic yolk syncytial layer (YSL) with a dorsal-to-ventral gradient (Fig. 4A and fig. S18). *spns2* expression in the YSL was strongly detected just below the developing myocardial precursors and was maintained throughout the segmentation period (Fig. 4, B to D). Recent evidence demonstrated that both endoderm and YSL regulate cardiac morphogenesis (*18*–*20*). Expression of the endoderm markers *sox17* and *foxa2* was not affected in *spns2*^{ko157} mutant embryos (fig. S3). In addition, *spns2* expression was not affected in endoderm-defective *casanova/sox32* morphants (fig. S18), which suggests that *spns2* expression in the YSL is regulated independently of the endoderm. *spns2* expression was detected in somites and in the tip of the tail at the 15-somite stage (fig. S18). We observed *spns2* expression in the myocardial precursors and in the intermediate cell mass (fig. S18). Thus, the expression of *spns2* is complex and dynamic. Although the overall morphology of the head and trunk appeared to be normal in the *spns2*^{ko157} mutant, we observed substantially increased apoptotic cells in the tail but not in the heart, head, and anterior trunk of the *spns2*^{ko157} mutant (fig. S19). These results suggest the involvement of Spns2 in the regulation of multiple organogenesis processes.

Because *spns2* was strongly expressed in the YSL below the developing myocardial precursors, we further examined whether Spns2 in the YSL contributes to the migration of myocardial precursors. When *spns2* MO (10 ng) was injected into the YSL at shield stage, cardia bifida was observed (Fig. 4, E and F, and table S5). In contrast, *mil* MO (15 ng) injection in the YSL at shield stage did not induce cardia bifida (Fig. 4,

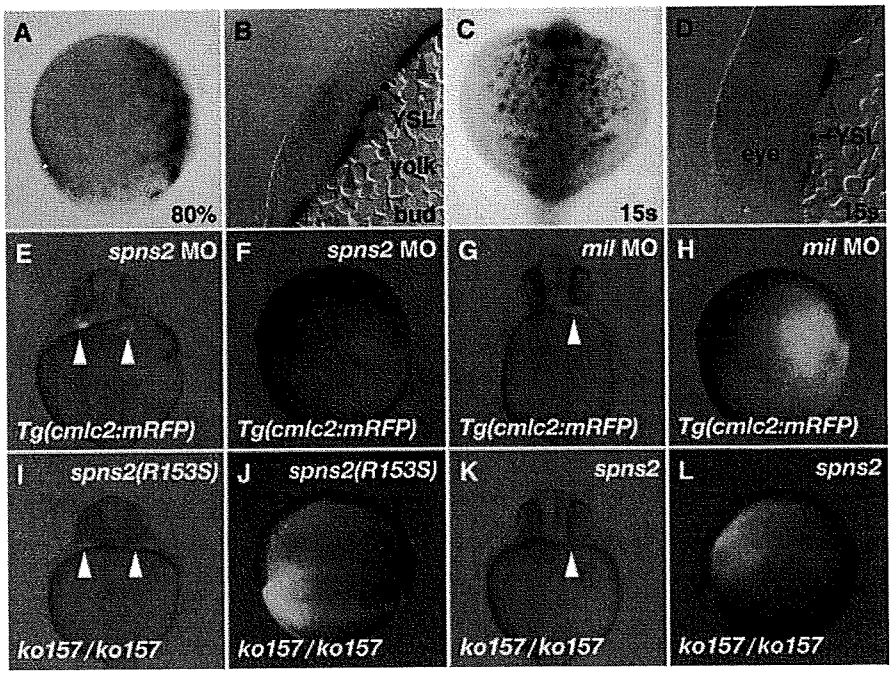

Fig. 4. Spns2 in the YSL is required for the migration of myocardial precursors. (**A** to **D**) Whole-mount in situ hybridization with antisense *spns2* probe at different stages of development. (B) and (D) show transverse sections of *spns2*-stained embryos. *spns2* was expressed in the YSL with a dorsal-to-ventral gradient at 80% epiboly stage [(A); dorsal right, lateral view]. *spns2* expression was maintained in the YSL at bud and 15s stages [(B) and (D); red arrowheads] and detected under the anterior midline [(C); dorsal up, anterior view]. (**E** to **H**) Injection of *spns2* MO (10 ng) with fluorescein isothiocyanate (FITC)–dextran into the YSL of shield-stage embryos led to cardia bifida, whereas injection of *mil* MO (15 ng) did not. (**I** to **L**) Cardia bifida in *spns2*^{ko157} mutant was recovered by mRNA injection of *spns2* (250 pg) with FITC-dextran into the YSL of shield-stage embryos but not by mRNA injection of *spns2(R153S)* (250 pg). Genotypes were confirmed by direct sequencing of the *ko157* locus. Injection into the YSL was confirmed by the distribution of FITC-dextran in the YSL at gastrulation stages [(F), (H), (J), and (L)]. White arrowheads indicate the positions of *cmlc2* expression domain [(E), (G), (I), and (K)].

G and H, and table S5). Because *mil/S1P2* is expressed in the mesoderm just lateral to the midline (*4*), *mil/S1P2* is proposed to function in mesoderm over the YSL. Further, cardia bifida in the *spns2*^{ko157} mutant was restored by the injection of *spns2* mRNA but not *spns2(R153S)* mRNA into the YSL at shield stage (Fig. 4, I to L, and table S6).

The rescue frequency by injection of *spns2* mRNA into the YSL was slightly lower than for injection into the blastomere (tables S2 and S6). One explanation is that *spns2* mRNA injected into the blastomere at the one-cell stage is widely distributed in the YSL because the YSL is constituted by marginal blastomeres collapsing onto the yolk around the 1000-cell stage. Another explanation is that the function of Spns2 in embryonic tissues as well as in the YSL may be partly required for the migration of myocardial precursors. Furthermore, transplantation analysis showed that Spns2 at least functions in a cell-nonautonomous manner, because *ko157*-derived donor cells were incorporated into single beating hearts of wild-type recipients, and wild type–derived donor cells were incorporated into one of two beating hearts of *ko157* recipients (movies S1 to S3). One attractive interpretation is that Spns2 in the YSL regulates the S1P export from the yolk to the embryonic body, leading to the activation of Mil/S1P$_2$ in mesoderm just lateral to the midline (fig. S1). Recent reports have pointed out the importance of *ferroportin1* (*fpn1*) as a transporter of iron from the yolk to the embryonic body (*21*) and the clinical relevance to hypochromic anemia and hemochromatosis in humans (*22*, *23*).

By investigating characteristic features of the zebrafish *spns2*^{ko157} mutant and analyzing the biological activity of Spns2, we have demonstrated that Spns2 functions as a S1P transporter and that Spns2 in the extraembryonic YSL is a prerequisite for the migration of myocardial precursors, presumably mediated by the S1P-Mil/S1P$_2$ pathway. The identification of Spns2 not only contributes to our understanding of the molecular mechanism of biological S1P delivery, but may also elucidate the physiological importance of Spns2 in autoimmune disease (*24*), cardiovascular diseases, and cancer (*25*) in which S1P plays a central role.

References and Notes

1. D. Y. Stainier, *Nat. Rev. Genet.* **2**, 39 (2001).
2. J. J. Schoenebeck, D. Yelon, *Semin. Cell Dev. Biol.* **18**, 27 (2007).
3. J. N. Chen, M. C. Fishman, *Trends Genet.* **16**, 383 (2000).
4. E. Kupperman, S. An, N. Osborne, S. Waldron, D. Y. Stainier, *Nature* **406**, 192 (2000).
5. M. J. Lee *et al.*, *Science* **279**, 1552 (1998).
6. T. Hla, *Pharmacol. Res.* **47**, 401 (2003).
7. S. Spiegel, S. Milstien, *Nat. Rev. Mol. Cell Biol.* **4**, 397 (2003).
8. Y. A. Hannun, L. M. Obeid, *Nat. Rev. Mol. Cell Biol.* **9**, 139 (2008).
9. T. Matsui *et al.*, *Nat. Clin. Pract. Cardiovasc. Med.* **4** (suppl. 1), S77 (2007).
10. Y. Nakano *et al.*, *Mol. Cell. Biol.* **21**, 3775 (2001).
11. R. M. Young *et al.*, *Dev. Dyn.* **223**, 298 (2002).
12. Y. Huang, M. J. Lemieux, J. Song, M. Auer, D. N. Wang, *Science* **301**, 616 (2003).
13. N. Kobayashi *et al.*, *J. Lipid Res.* **47**, 614 (2006).
14. P. Mitra *et al.*, *Proc. Natl. Acad. Sci. U.S.A.* **103**, 16394 (2006).
15. K. Sato *et al.*, *J. Neurochem.* **103**, 2610 (2007).
16. E. B. Neufeld *et al.*, *J. Biol. Chem.* **276**, 27584 (2001).
17. Y. M. Lee, K. Venkataraman, S. I. Hwang, D. K. Han, T. Hla, *Prostaglandins Other Lipid Mediat.* **84**, 154 (2007).
18. Y. Kikuchi *et al.*, *Genes Dev.* **15**, 1493 (2001).
19. T. Dickmeis *et al.*, *Genes Dev.* **15**, 1487 (2001).
20. T. Sakaguchi, Y. Kikuchi, A. Kuroiwa, H. Takeda, D. Y. Stainier, *Development* **133**, 4063 (2006).
21. A. Donovan *et al.*, *Nature* **403**, 776 (2000).
22. O. T. Njajou *et al.*, *Nat. Genet.* **28**, 213 (2001).
23. G. Montosi *et al.*, *J. Clin. Invest.* **108**, 619 (2001).
24. M. Sekiguchi *et al.*, *J. Immunol.* **180**, 1921 (2008).
25. S. Milstien, S. Spiegel, *Cancer Cell* **9**, 148 (2006).

26. We thank M. Sone and M. Minamimoto for technical assistance; S. Endo and R. Hanaoka for the mutagenesis screening; T. Kitaguchi for the establishment of cmlc2:mRFP; M. Masuda, Y. Igarashi, A. Kihara, S. Mitsutake, K. Shioya, I. B. Dawid, and Y. Kaziro for support and suggestions; M. Hibi, J. S. Gutkind, and M. Tsang for critical reading and valuable suggestions; D. Y. Stainier for discussions and sharing of unpublished data; and H. Okamoto, K. Kawakami, Y. Kikuchi, H. Yanagisawa, D. Yamamoto, R. Y. Tsien, and H.-J. Tsai for fish and reagents. Supported by grants from the Ministry of Education, Culture, Sports, Science and Technology of Japan; the National BioResource Project of Japan; the Japan Society for the Promotion of Science; the Program for the Promotion of Fundamental Studies in Health Sciences of the National Institute of Biomedical Innovation; the Ministry of Health, Labor and Welfare of Japan; and the Takeda Science Foundation. The sequences of zebrafish *spns2*, human *Spns2*, and mouse *Spns2* have been deposited in the DNA Data Bank of Japan [accession numbers: AB441164 (zebrafish), AB441165 (human), AB441166 (mouse)]. The authors are filing a patent based on the results reported in this paper.

Supporting Online Material

www.sciencemag.org/cgi/content/full/1167449/DC1
Materials and Methods
Figs. S1 to S19
Tables S1 to S6
Movies S1 to S3
References

20 October 2008; accepted 3 December 2008
Published online 11 December 2008;
10.1126/science.1167449
Include this information when citing this paper.

The Peopling of the Pacific from a Bacterial Perspective

Yoshan Moodley,[1*†] Bodo Linz,[1*‡] Yoshio Yamaoka,[2*] Helen M. Windsor,[3] Sebastien Breurec,[4,5] Jeng-Yih Wu,[6] Ayas Maady,[7] Steffie Bernhöft,[1] Jean-Michel Thiberge,[8] Suparat Phuanukoonnon,[9] Gangolf Jobb,[10] Peter Siba,[9] David Y. Graham,[2] Barry J. Marshall,[3] Mark Achtman[1,11§]

Two prehistoric migrations peopled the Pacific. One reached New Guinea and Australia, and a second, more recent, migration extended through Melanesia and from there to the Polynesian islands. These migrations were accompanied by two distinct populations of the specific human pathogen *Helicobacter pylori*, called hpSahul and hspMaori, respectively. hpSahul split from Asian populations of *H. pylori* 31,000 to 37,000 years ago, in concordance with archaeological history. The hpSahul populations in New Guinea and Australia have diverged sufficiently to indicate that they have remained isolated for the past 23,000 to 32,000 years. The second human expansion from Taiwan 5000 years ago dispersed one of several subgroups of the Austronesian language family along with one of several hspMaori clades into Melanesia and Polynesia, where both language and parasite have continued to diverge.

After modern humans dispersed "out of Africa" about 60,000 years ago (60 ka) (*1*), they reached Asia via a southern coastal route (*2*). That route extended along the Pleistocene landmass, known as Sundaland (i.e., the Malay peninsula, Sumatra, Java, Borneo, and Bali), that was joined to the Asian mainland as a result of low sea levels during the last ice age (12 to 43 ka) (*3*). Low sea levels also meant that Australia, New Guinea, and Tasmania were connected in a continent called Sahul, separated from Sundaland by a few narrow deep-sea channels. It seems Sahul was colonized only once, ~40 to 50 ka (*3*, *4*), although backed-blade stone tool technology and the dingo appear to have been introduced from India at a later date (*5*, *6*).

[1]Max-Planck-Institut für Infektionsbiologie, Department of Molecular Biology, Charitéplatz 1, 10117 Berlin, Germany. [2]Department of Medicine-Gastroenterology, Baylor College of Medicine and Michael E. DeBakey VA Medical Center, Houston, TX 77030, USA. [3]Microbiology and Immunology M502, School of Biomedical, Biomolecular and Chemical Sciences, University of Western Australia, Australia 6009. [4]Institut Pasteur, BP 220, Dakar, Sénégal. [5]Institut Pasteur de Nouvelle-Calédonie, BP61, 98845 Noumea, New Caledonia. [6]Department of Gastroenterology, Kaohsiung Medical University, 100 Shih-Chuan 1st Road, Kaohsiung 80708, Taiwan. [7]Department of Endoscopy, Republic Hospital No. 1, Kyzyl City 667003, Republic of Tuva, Russia. [8]Institut Pasteur, Genotyping of Pathogens and Public Health, 28 rue du Dr Roux, 75724 Paris, France. [9]Papua New Guinea Institute of Medical Research, Post Office Box 60, Goroka, EHP, 441 Papua New Guinea. [10]Fritz-Kortner-Bogen 36, 81739 Munich, Germany. [11]Environmental Research Institute and Department of Microbiology, University College Cork, Cork, Ireland.

*These authors contributed equally to this work.
†Present address: Austrian Academy of Sciences, Konrad Lorenz Institute for Ethology, Savoyenstrasse 1A, A-1160, Vienna, Austria.
‡Present address: Department of Biochemistry and Molecular Biology, Pennsylvania State University, University Park, PA 16802, USA.
§To whom correspondence should be addressed. E-mail: m.achtman@ucc.ie

Cell Metabolism
Article

Angiopoietin-like Protein 2 Promotes Chronic Adipose Tissue Inflammation and Obesity-Related Systemic Insulin Resistance

Mitsuhisa Tabata,[1,13] Tsuyoshi Kadomatsu,[1] Shigetomo Fukuhara,[7] Keishi Miyata,[1] Yasuhiro Ito,[1,2] Motoyoshi Endo,[1] Takashi Urano,[1,2] Hui Juan Zhu,[1] Hiroto Tsukano,[1] Hirokazu Tazume,[1] Koichi Kaikita,[3] Kazuya Miyashita,[8] Takao Iwawaki,[9] Michio Shimabukuro,[10] Kazuhiko Sakaguchi,[11] Takaaki Ito,[5] Naomi Nakagata,[6] Tetsuya Yamada,[12] Hideki Katagiri,[12] Masato Kasuga,[11,16] Yukio Ando,[4] Hisao Ogawa,[3] Naoki Mochizuki,[7] Hiroshi Itoh,[13] Toshio Suda,[14] and Yuichi Oike[1,15,*]

[1]Department of Molecular Genetics
[2]Department of Ophthalmology and Visual Science
[3]Department of Cardiovascular Medicine
[4]Department of Diagnostic Medicine
[5]Department of Pathology and Experimental Medicine
Graduate School of Medical Sciences, Kumamoto University, 1-1-1 Honjo, Kumamoto 860-8556, Japan
[6]Center for Animal Resources and Development, Kumamoto University, 2-2-1 Honjo, Kumamoto 860-0811, Japan
[7]Department of Structural Analysis, National Cardiovascular Center Research Institute, Suita, Osaka 565-8565, Japan
[8]Immuno-Biological Laboratories Co., Ltd., Aramachi, Takasaki 370-0831, Japan
[9]Initiative Research Unit, RIKEN Advanced Science Institute, Wako 351-0189, Japan
[10]Second Department of Internal Medicine, University of the Ryukyu, Okinawa 903-0215, Japan
[11]Division of Diabetes, Metabolism, and Endocrinology, Department of Internal Medicine, Kobe University Graduate School of Medicine, Chuo-ku, Kobe 650-0017, Japan
[12]Division of Molecular Medicine and Diabetes, Tohoku University Graduate School of Medicine, Aoba-ku, Sendai 980-8575, Japan
[13]Division of Endocrinology, Metabolism, and Nephrology, Department of Internal Medicine
[14]Department of Cell Differentiation, The Sakaguchi Laboratory
School of Medicine, Keio University, Shinjuku-ku, Tokyo 160-8582, Japan
[15]PRESTO, Japan Science Technology Agency, Kawaguchi, Saitama 332-0012, Japan
[16]Present address: Research Institute, International Medical Center of Japan, Shinjuku-ku, Tokyo 162-8655, Japan
*Correspondence: oike@gpo.kumamoto-u.ac.jp
DOI 10.1016/j.cmet.2009.08.003

SUMMARY

Recent studies of obesity have provided new insights into the mechanisms underlying insulin resistance and metabolic dysregulation. Numerous efforts have been made to identify key regulators of obesity-linked adipose tissue inflammation and insulin resistance. We found that angiopoietin-like protein 2 (Angptl2) was secreted by adipose tissue and that its circulating level was closely related to adiposity, systemic insulin resistance, and inflammation in both mice and humans. Angptl2 activated an inflammatory cascade in endothelial cells via integrin signaling and induced chemotaxis of monocytes/macrophages. Constitutive Angptl2 activation in vivo induced inflammation of the vasculature characterized by abundant attachment of leukocytes to the vessel walls and increased permeability. Angptl2 deletion ameliorated adipose tissue inflammation and systemic insulin resistance in diet-induced obese mice. Conversely, Angptl2 overexpression in adipose tissue caused local inflammation and systemic insulin resistance in nonobese mice. Thus, Angptl2 is a key adipocyte-derived inflammatory mediator that links obesity to systemic insulin resistance.

INTRODUCTION

Obesity is a pandemic medical and social problem that is associated with several adverse health outcomes, including type 2 diabetes, hypertension, dyslipidemia, cardiovascular disease, and cancer (Eckel et al., 2005; Mokdad et al., 2003), all of which result in increased mortality. A major metabolic manifestation of obesity is systemic insulin resistance. Recently, the concept has emerged that chronic low-grade activation of proinflammatory pathways in adipose tissue directly promotes systemic insulin resistance (Apovian et al., 2008; Neels and Olefsky, 2006; Schenk et al., 2008). Adipocytes and macrophages could be a source of several proinflammatory cytokines that activate inflammatory pathways in resident and infiltrating cells within adipose tissue in a paracrine or autocrine fashion (Kanda et al., 2006; Weisberg et al., 2006). However, the molecular mechanisms underlying inflammation of adipose tissue in obesity have not fully clarified.

Fibrinogen promotes leukocyte adhesion and cytokine secretion at sites of inflammation through integrin-dependent inflammatory pathways (Herrick et al., 1999; Mosesson, 2005).

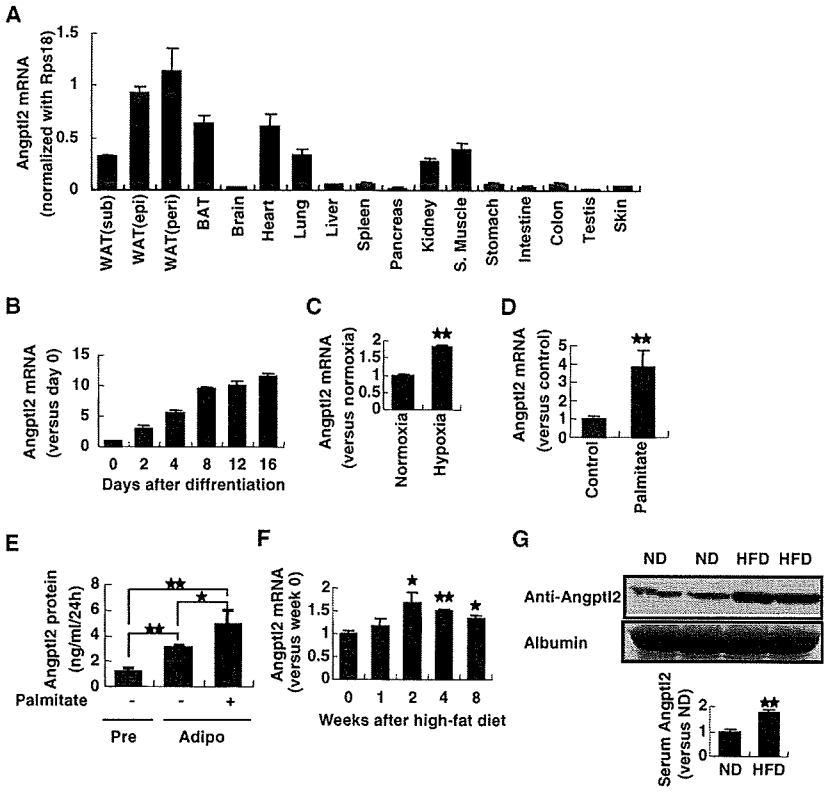

Figure 1. Angptl2 Is Secreted by Adipose Tissue

(A) Angptl2 mRNA expression in various tissues of mice fed normal chow (n = 4). WAT, white adipose tissue; sub, subcutaneous; peri, perirenal; mes, mesenteric; BAT, brown adipose tissue; S. Muscle, skeletal muscle.

(B–D) Angptl2 mRNA expression in 3T3-L1 cells during adipocyte differentiation (n = 3) (B), in differentiated 3T3-L1 cells incubated under hypoxic conditions (1% O_2, 24 hr, n = 3) (C), and in cells treated with palmitate (200 μM, 24 hr, n = 4) (D).

(E) Angptl2 protein levels in culture medium of pre- (Pre) or postdifferentiated (Adipo) 3T3-L1 cells with or without palmitate treatment (200 μM, 24 hr, n = 4).

(F) Angptl2 mRNA expression in the mesenteric adipose tissue of obese mice fed a high-fat diet for the indicated periods starting at 8 weeks of age (n = 4).

(G) Representative western blot and quantitative evaluation of serum Angptl2 protein in mice fed a normal diet (ND) or a high-fat diet (HFD) for a period of 8 weeks (n = 4). CBB-stained albumin is as control bands for protein loading. Data are the mean ± SEM, *p < 0.05 and **p < 0.01 compared with controls.

Fibrinogen-binding integrins are abundantly expressed by monocytes/macrophages and endothelial cells, and fibrinogen must undergo oligomerization or polymerization to display its activity. The presence of extravascular fibrinogen at sites of inflammation has been documented by pathologists for decades (Dvorak et al., 1985). These findings prompted us to ask whether an oligomeric protein derived from adipose tissue and containing a fibrinogen-like sequence might play a pathological role in inflammatory changes of adipose tissue associated with obesity. Recently, we and others identified seven angiopoietin-like proteins (Angptls), which possess a coiled-coil domain at the N terminus for oligomerization and a C-terminal fibrinogen-like domain (Kim et al., 1999; Kubota et al., 2005a; Oike et al., 2004). Angptls are structurally similar to Tie-2 receptor ligands (angiopoietins), but Angptls do not bind to either Tie2 or the homologous Tie1 protein, indicating that their role differs from that of angiopoietins.

Here we show that angiopoietin-like protein 2 (Angptl2) is primarily secreted by adipose tissue and that its expression is increased by obesity and obesity-related pathological conditions, including hypoxia and endoplasmic reticulum (ER) stress. We found that increased circulating Angptl2 levels were closely related to adiposity, systemic insulin resistance, and inflammation in both mice and humans. Angptl2 acted on endothelial cells and monocytes/macrophages via integrin signaling, resulting in the promotion of inflammation. Constitutive activation of Angptl2 in mouse skin tissue induced chronic inflammation, including inflammatory changes of the vasculature characterized by abundant attachment of leukocytes to the vessel walls and increased permeability. Deletion of Angptl2 led to reduced inflammation in adipose tissue and ameliorated systemic insulin resistance in mice with dietary obesity. Conversely, persistent overexpression of Angptl2 in adipose tissue caused local inflammation and systemic insulin resistance in nonobese mice. These findings establish Angptl2 as a key adipocyte-derived inflammatory mediator linking obesity to systemic insulin resistance and identify it as a new molecular target that could be used to improve the diagnosis and treatment of obesity and related metabolic diseases.

RESULTS

Angptl2 Expression in White Adipose Tissue Is Increased by Obesity and Obesity-Related Stress

Angptl2 mRNA was widely expressed in various organs of mice, but its level was particularly elevated in visceral white adipose tissues (Figure 1A). Differentiated 3T3-L1 adipocytes expressed Angptl2 mRNA (Figure 1B), and its expression was increased by hypoxia (Figure 1C), which occurs in obese adipose tissue (Hosogai et al., 2007; Nishimura et al., 2008; Schenk et al., 2008; Ye, 2009). We found significantly increased ER stress in adipocytes from obese mice compared with cells from nonobese mice (see Figure S1 available online). Serum levels of long-chain saturated fatty acids (LCSFAs) are elevated in obesity, and LCSFAs promote ER stress in adipocytes (Schenk et al., 2008). Our in vitro study of cultured 3T3-L1 cells revealed that ER stress was induced in adipocytes after treatment with palmitate, one of the LCSFA, or thapsigargin, an ER stress inducer. As

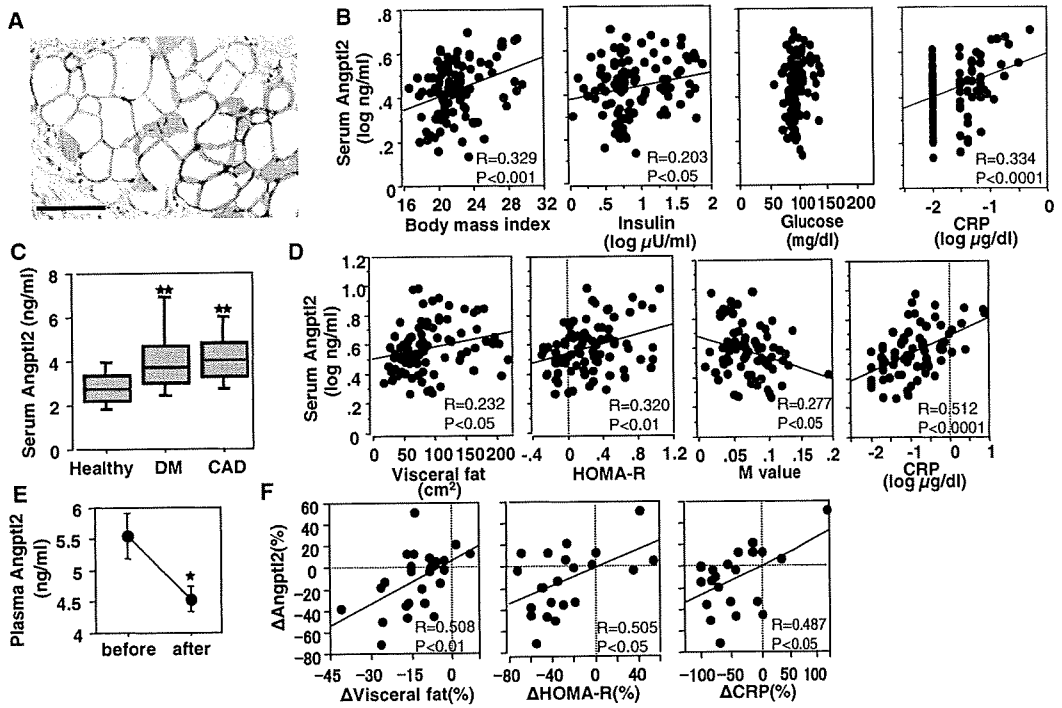

Figure 2. Circulating Angptl2 Is Correlated with Adiposity, Insulin Resistance, and Inflammation in Humans

(A) Immunohistochemical staining for Angptl2 in human adipose tissue. Scale bar, 100 μm.

(B) Correlation of the serum Angptl2 level with the body mass index or serum insulin, glucose, and CRP levels in healthy volunteers (n = 98).

(C) Serum Angptl2 levels in healthy volunteers (Healthy, n = 98) and in patients with type 2 diabetes (DM, n = 89) or coronary artery disease (CAD, n = 109). Horizontal bars represent the 10%–90% percentile range, and boxes indicate the 25%–75% percentile range. The horizontal line in each box corresponds to the median.

(D) Correlation of the serum Angptl2 level with the visceral fat area, HOMA-R index, M value, and CRP level in diabetic patients.

(E and F) Changes of the plasma Angptl2 level in obese diabetic male patients after pioglitazone treatment (n = 27). Plasma Angptl2 levels (mean ± SEM) before and after treatment (E). Correlation of the change (%) of the plasma Angptl2 level with the change (%) of the visceral fat area, subcutaneous fat area, HOMA-R index, and CRP level. Correlation coefficient (R) and probability (P) values are shown (F). *$p < 0.05$ and **$p < 0.01$ compared with controls.

a result, both the cellular Angptl2 mRNA level and its protein concentration in the culture medium were significantly increased (Figures 1D and 1E, Figure S2, and data not shown). Angptl2 mRNA in mesenteric white adipose tissue and serum Angptl2 protein levels were increased in obese mice fed a high-fat diet (Figures 1F and 1G), suggesting that Angptl2 is a bioactive adipocyte-derived factor that has a role in obesity and related metabolic diseases.

Circulating Angptl2 Level Is Correlated with Adiposity, Systemic Insulin Resistance, and Inflammation in Humans

Immunohistochemical analysis revealed that Angptl2 was expressed by the adipocytes of human adipose tissue (Figure 2A). We analyzed the circulating levels of Angptl2 in various human subjects by using an enzyme-linked immunosorbent assay (ELISA). In healthy normal-weight volunteers aged from 20 to 59 years, the serum Angptl2 concentration ranged from 1.36 to 4.98 ng/ml, and the distribution was normal after log transformation (Figure S3A). Plasma levels were comparable and strongly correlated with the corresponding serum levels (Figure S3B). There was no significant difference of serum Angptl2 concentration between genders (data not shown). Angptl2 level showed a positive correlation with body mass index, serum insulin level, and serum C-reactive protein (CRP) level. In contrast, the level of Angptl4, which has already been identified as an adipocyte-derived Angptl, showed no correlation with these factors in normal-weight healthy subjects (Figure 2B and Figure S4). An increase of the body mass index, serum insulin level, and CRP level is associated with the development of type 2 diabetes and atherosclerosis (Eckel et al., 2005; Mokdad et al., 2003). Indeed, serum Angptl2 was also significantly increased in patients with type 2 diabetes or coronary artery disease (Figure 2C). In 935 consecutive persons aged 27–84 years who underwent a medical checkup and gave informed consent for measurement of serum Angptl2 at the Japanese Red Cross Kumamoto Health Care Center, the Angptl2 level was positively correlated with the body mass index, abdominal circumference, and serum CRP level (Figure S5). In patients with type 2 diabetes, Angptl2 was positively correlated with the visceral fat area, homeostasis model assessment of insulin resistance (HOMA-R) index (Matthews et al., 1985), and serum CRP level, but not with the subcutaneous fat area. Angptl2 level was inversely correlated with the insulin sensitivity index (M value), as assessed

by the hyperinsulinemic euglycemic clamp test (DeFronzo et al., 1979) (Figure 2D).

These observations led us to ask whether improvement of systemic insulin resistance or inflammation would influence the circulating level of Angptl2. We observed a significant decrease of the plasma Angptl2 level in 27 obese diabetic men following treatment with pioglitazone at 30 mg/day for 3 months (Figure 2E). The percent decrease of the plasma Angptl2 level was correlated with the percent decrease of the visceral fat area, HOMA-R index, and serum CRP level (Figure 2F). These results suggested that visceral fat was likely to be the main source of circulating Angptl2, the concentration of which was significantly correlated with systemic insulin resistance and inflammation.

Angptl2 Activates Migration and Inflammatory Changes of Endothelial Cells and Monocytes/Macrophages via Integrins

Since the vasculature has an important role in tissue inflammation (Jackson et al., 1997), we examined the effect of Angptl2 on endothelial cells. First, we found a dose-dependent increase of cell adhesion when human umbilical vein endothelial cells (HUVECs) and human arterial endothelial cells (HAECs), which express several integrins on their surfaces, were plated on Angptl2-coated plates (Figures 3A and S6). We next analyzed cell adhesion in the presence of a series of function-blocking antibodies for specific integrins. A neutralizing antibody for integrin $\alpha5\beta1$ inhibited endothelial cell adhesion to Angptl2-coated plates, as did RGD peptide, which blocks RGD-dependent integrins (Figure 3B), suggesting that Angptl2-induced endothelial cell adhesion was an $\alpha5\beta1$-dependent process, although the involvement of untested integrins could not be excluded. Integrin $\alpha5\beta1$ activates NF-κB in endothelial cells (Klein et al., 2002). Consistently, there was increased translocation of NF-κB to the nucleus and degradation of IκB in HUVECs stimulated with recombinant human Angptl2 protein (Figures 3C and 3D).

Angptl2 also promoted the migration of HUVECs and HAECs through a microchemotaxis membrane (Figure 3E). Time-lapse imaging of HUVECs or HAECs cultures revealed that protrusion of lamellipodia and membrane ruffling were rapidly induced following the addition of Angptl2 (Movies S1 and S2). Since Rac1, a small Rho-GTPase, plays a pivotal role in the protrusion of lamellipodia, membrane ruffling, and cell migration (Bar-Sagi and Hall, 2000; Fryer and Field, 2005), we investigated whether Rac1 was activated in HAECs and HUVECs by performing a pull-down assay. Activation of Rac1 was detected in both Angptl2-stimulated HUVECs and HAECs (Figure 3F). In viable Angptl2-stimulated HUVECs, a single-molecule probe was used to determine Rac1 activity, showing that it was diffusely activated at the plasma membrane, with this activation being followed by protrusion of lamellipodia and membrane ruffling (Figure 3G and Movie S3). Moreover, Angptl2 no longer stimulated the protrusion of lamellipodia and membrane ruffling in HUVECs transfected with a dominant-negative Rac1 mutant expressing red fluorescent protein (RacN17-IRES-RFP) (Figure 3H and Movie S4). These findings suggest that Angptl2-stimulated lamellipodia formation and membrane ruffling in endothelial cells were both mediated by activation of Rac1. Next, we investigated whether Angptl2 could induce in vivo chemotaxis of endothelial cells in a mouse cornea assay. Implanted pellets containing Angptl2 markedly induced neovascularization in the mouse cornea, whereas pellets containing PBS alone did not (Figure 3I). Monocytes/macrophages express several integrin receptors that are responsible for adhesion, migration, and extravasation into the peripheral tissues (Friedl and Weigelin, 2008; Rose et al., 2007). We found that the THP-1 human monocytic cell line expressed integrins $\alpha4$, $\beta1$, $\beta2$, and $\alpha5\beta1$ (Figure 3J). THP-1 cells adhered to Angptl2-coated plates in a dose-dependent manner (Figure 3K). FACS analysis revealed that Angptl2 bound to THP-1; this binding was completely inhibited by neutralizing antibodies for integrins $\alpha4$ or $\beta2$ and was partially blocked by antibodies for integrin $\alpha5\beta1$ or $\beta1$ (Figure 3L). Angptl2 also promoted transmigration by THP-1 cells and primary human monocytes (Figure 3M and Figure S7).

Constitutive Angptl2 Activation Induces Local Inflammation in Mouse Skin Tissue

To further investigate the role of Angptl2 in the inflammatory process, we generated transgenic mice expressing Angptl2 driven by the keratinocyte-specific promoter K14 (K14-Angptl2) and therefore constitutively expressing Angptl2 in the epidermis (Figures S8A and S8B). The ears, snouts, and eyelids of K14-Angptl2 mice were redder than those of controls. The tails of K14-Angptl2 mice were not only reddish but also swollen and showed loss at the tips (Figure 4A), indicating local inflammation. Lectin staining showed an increase of adherent leukocytes, a common feature of inflammatory vasculature (McDonald, 1994), in enlarged vessels of the skin tissue specimens from K14-Angptl2 mice (Figure 4B), while there was no difference of vessel length between the genotypes (Figure S8C). The vessels of K14-Angptl2 mice were significantly more permeable than the vessels of wild-type controls after inflammation was induced by topical application of mustard oil, a potent proinflammatory agent (Figure 4C). As expected, even before mustard oil application, lumens of $CD31^+LYVE\text{-}1^+$ lymphatics were enlarged in the skin of K14-Angptl2 mice, while such changes were not observed in controls (Figure 4D), suggesting that increased drainage via lymphatics was compensating for the excessive leakiness of Angptl2-stimulated vessels in the dermis. These findings indicate that Angptl2 induces inflammatory vascular remodeling rather than angiogenesis.

Reduction of Adiposity and Obesity-Related Adipose Tissue Inflammation in *Angptl2*$^{-/-}$ Mice

Next, we investigated the pathophysiological role of Angptl2 by generating Angptl2 knockout (*Angptl2*$^{-/-}$) mice (Figure S9). *Angptl2*$^{-/-}$ mice were born alive following Mendelian inheritance and appeared to be grossly normal. Interestingly, when fed normal chow, *Angptl2*$^{-/-}$ mice weighed slightly less (Figure S10A) and had a lower body fat mass estimated by computed tomography (CT) (Figures S10B and S10C) than heterozygotes or wild-type mice fed the same normal diet, although there was no significant difference of daily food intake or energy expenditure between the groups (Figures S10D and S10E). In addition, *Angptl2*$^{-/-}$ mice showed slightly, but significant, better glucose tolerance and insulin sensitivity (Figures S10F and S10G). Next, we fed 8-week-old mice a high-fat diet containing 32% (wt/wt) fat to stimulate weight gain. After

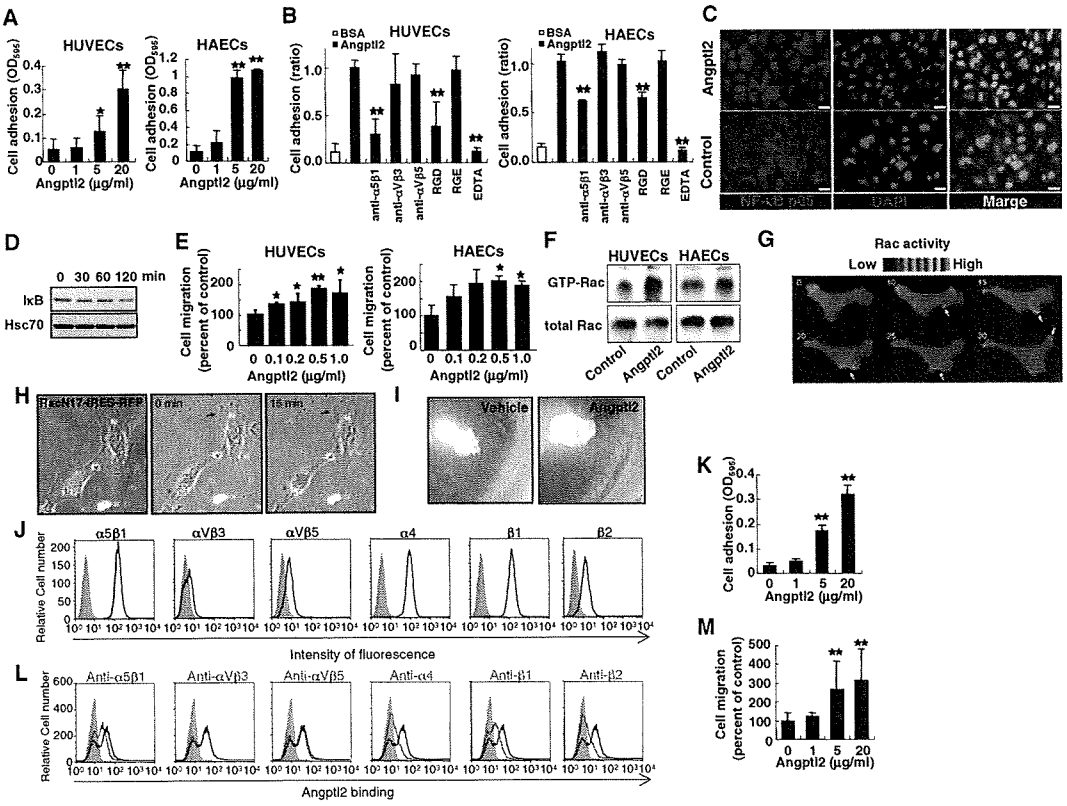

Figure 3. Angptl2 Activates Endothelial Cells and Monocytes

(A) Adhesion of HUVECs or HAECs to culture dishes coated with various concentrations of recombinant human Angptl2 (n = 3).

(B) HUVECs or HAECs were preincubated with or without 25 μg/ml of blocking antibodies (anti-α5β1, anti-αvβ3, or anti-αvβ5) or RGD or RGE peptides (300 μM), and cell adhesion was assessed (n = 3). As a negative control, cell adhesion was assayed in the presence of 10 μM EDTA, which inhibits integrin binding.

(C) Nuclear translocation of NF-κB subunit p65 in HUVECs at 2 hr after Angptl2 stimulation. Nuclei were counterstained with 4′,6′-diamidino-2-phenylindole (DAPI). Scale bar, 20 μm.

(D) Representative western blots of IκB and Hsc70 protein (internal control) in HUVECs at the indicated times after Angptl2 stimulation.

(E) Migration of HUVECs or HAECs in response to Angptl2 (n = 4).

(F) HUVECs or HAECs were cultured with Angptl2 for 30 min and then subjected to the pull-down assay using GST-PAK-CRIB followed by western blotting with anti-Rac1 antibody. Representative images are shown.

(G) HUVECs expressing Raichu-Rac1 (a probe for active Rac1) at the indicated times (min) after Angptl2 stimulation. Arrows indicate nascent and retracting lamellipodia. Ratio ranges are shown on the right.

(H) HUVECs that were either untransfected or transfected with RacN17 (shown in red in the left panel and by red stars in the center and right panels) and stimulated with Angptl2 at time 0 and 15 min. Angptl2-stimulated membrane ruffling is observed in HUVECs without RacN17 (arrows).

(I) Macroscopic appearance of neovascularization in the mouse cornea. Pellets containing vehicle or Angptl2 (0.5 μg) were implanted into micropockets cut in the corneal stroma.

(J) Integrin expression by THP-1 cells. Typical profiles obtained by FACS analysis with the indicated anti-integrin antibodies (black line traces) or isotype-matched control IgG (filled gray traces).

(K) Adhesion of THP-1 cells to culture dishes coated with various concentrations of Angptl2 (n = 3).

(L) Inhibition of Angptl2 binding to THP-1 cells by integrin-neutralizing antibodies. THP-1 cells were preincubated with (red line traces) or without (blue line traces) the indicated anti-integrin neutralizing antibodies, and then incubated with FLAG-tagged Angptl2 followed by detection with FITC-conjugated anti-FLAG antibody. Negative controls (filled gray traces) had omission of Angptl2.

(M) Migration of THP-1 cells in response to Angptl2 (n = 7–9). Data are the mean ± SD, *$p < 0.05$ and **$p < 0.01$ compared with controls.

8 weeks of high-fat diet feeding, *Angptl2*$^{-/-}$ mice had a body weight 12% lower than that of wild-type mice (Figure 5A). The visceral and subcutaneous fat mass and total body fat percentage were moderately decreased in *Angptl2*$^{-/-}$ mice compared to wild-type mice (Figures 5B and 5C). Considerable accumulation of fat was seen in the liver and skeletal muscle of wild-type mice, whereas these changes were mild in *Angptl2*$^{-/-}$ mice (Figures 5D and 5E). Although there were no obvious differences of food intake or energy expenditure between the two groups, the respiratory quotient was significantly lower in the *Angptl2*$^{-/-}$ group (Figures S11A–S11C).

We next examined the expression of mRNAs for inflammatory cytokines (IL-6 and TNF-α), a chemokine (MCP-1), various macrophage markers (F4/80, CD68, CCR2, Mgl1, and Mgl2),

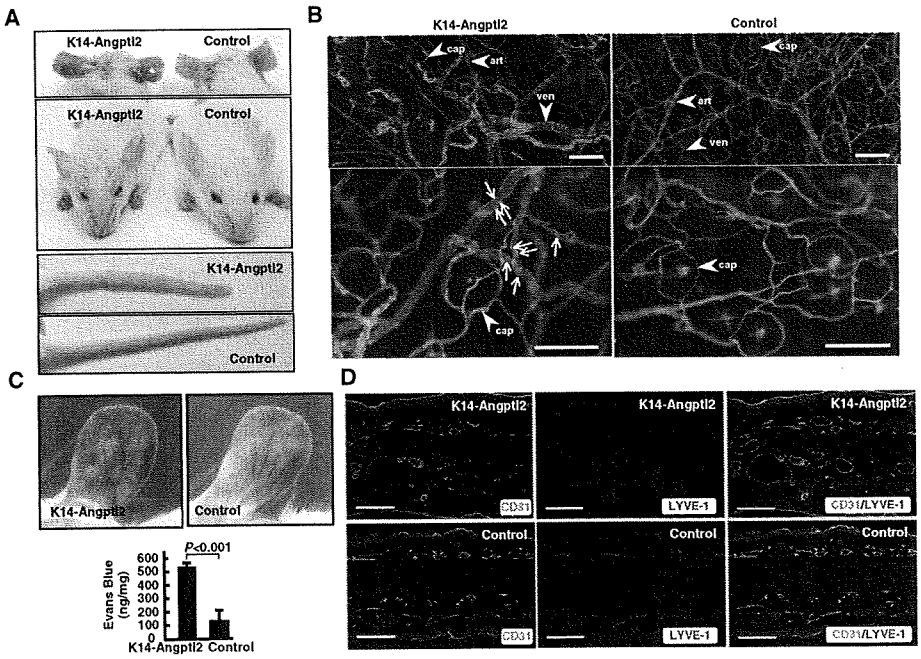

Figure 4. Sustained Angptl2 Overexpression Induces Vascular Inflammation

(A) Appearance of 6-month-old transgenic K14-Angptl2 and control mice.

(B) Ear skin blood vessels from transgenic and control mice. Arrows indicate adherent leukocytes on the walls of enlarged vessels from K14-Angptl2 mice. Arrowheads with art, ven, and cap in each panel indicate arteriole, venule, and capillary, respectively. Scale bar, 200 μm.

(C) Evans blue dye leakage into the skin of the ear following treatment with mustard oil as an inflammatory agent. Representative images and quantitative values are shown (mean ± SD, n = 7).

(D) Immunohistochemistry of ear skin from K14-Angptl2 and control mice with anti-CD31 and anti-LYVE-1 antibodies. Representative photographs are shown. Scale bar, 100 μm.

and insulin-sensitizing adipocytokines (adiponectin and leptin) in the adipose tissue of mice fed a high-fat diet. As shown in Figure 5F, adiponectin expression was increased, while TNF-α and general (F4/80, CD68) and inflammatory (CCR2) macrophage markers were all decreased in the adipose tissue of *Angptl2*$^{-/-}$ mice. However, the expression of residential macrophage markers (Mgl1 and Mgl2) remained unchanged. Furthermore, expression of F4/80 mRNA was positively correlated with the adipose tissue weight in controls, indicating that adiposity was significantly correlated with macrophage infiltration into adipose tissue. In contrast, there was no significant correlation between adipose tissue weight and macrophage infiltration in *Angptl2*$^{-/-}$ mice (Figure 5G), suggesting that this decrease of macrophage infiltration may be independent of reduced adiposity in *Angptl2*$^{-/-}$ mice. Furthermore, immunohistochemistry using the macrophage marker Mac2 revealed accumulation of Mac2-positive macrophages in crown-like structures within the adipose tissue of wild-type mice, while fewer Mac2-positive cells were observed in the adipose tissue of *Angptl2*$^{-/-}$ mice (Figure 5H). The high-fat diet caused impaired glucose tolerance and insulin resistance in controls, whereas *Angptl2*$^{-/-}$ mice showed better glucose tolerance and insulin sensitivity based on the results of intraperitoneal glucose and insulin tolerance tests (GTT and ITT, respectively) (Figures 5I and 5J). To explore which organ(s) contributed to the improved insulin sensitivity in *Angptl2*$^{-/-}$ mice, we next performed western blotting analysis of the insulin signaling pathway. Tyrosine phosphorylation of insulin receptor β and serine phosphorylation of Akt after insulin injection were significantly increased in both the liver and skeletal muscle of *Angptl2*$^{-/-}$ mice compared with wild-type mice (Figure 5K). To confirm these results, we performed hyperinsulinemic-euglycemic clamp experiments. Both glucose infusion rate and whole-body glucose disposal rate were significantly increased in *Angptl2*$^{-/-}$ mice, while clamp endogenous glucose production was significantly reduced. In addition, the percent decrease in endogenous glucose production from basal to clamp states was significantly higher in *Angptl2*$^{-/-}$ mice than in wild-type mice (Figure 5L). These results indicated that insulin sensitivity was improved in both the skeletal muscle and liver of *Angptl2*$^{-/-}$ mice fed a high-fat diet.

Angptl2 Promotes Local Inflammation in Adipose Tissue and Systemic Insulin Resistance

Finally, we determined whether sustained overexpression of Angptl2 in adipose tissue promoted systemic insulin resistance by generating transgenic mice that overexpressed Angptl2 in adipose tissue under the control of aP2, an adipose tissue-specific promoter (aP2-Angptl2) (Figure S12A). Based on the level of Angptl2 expression, we considered that line 5 was the most acceptable model for examining the pathological role of increased Angptl2 expression in obese mice (Figure S12B), so we performed subsequent analyses using line 5 and wild-type

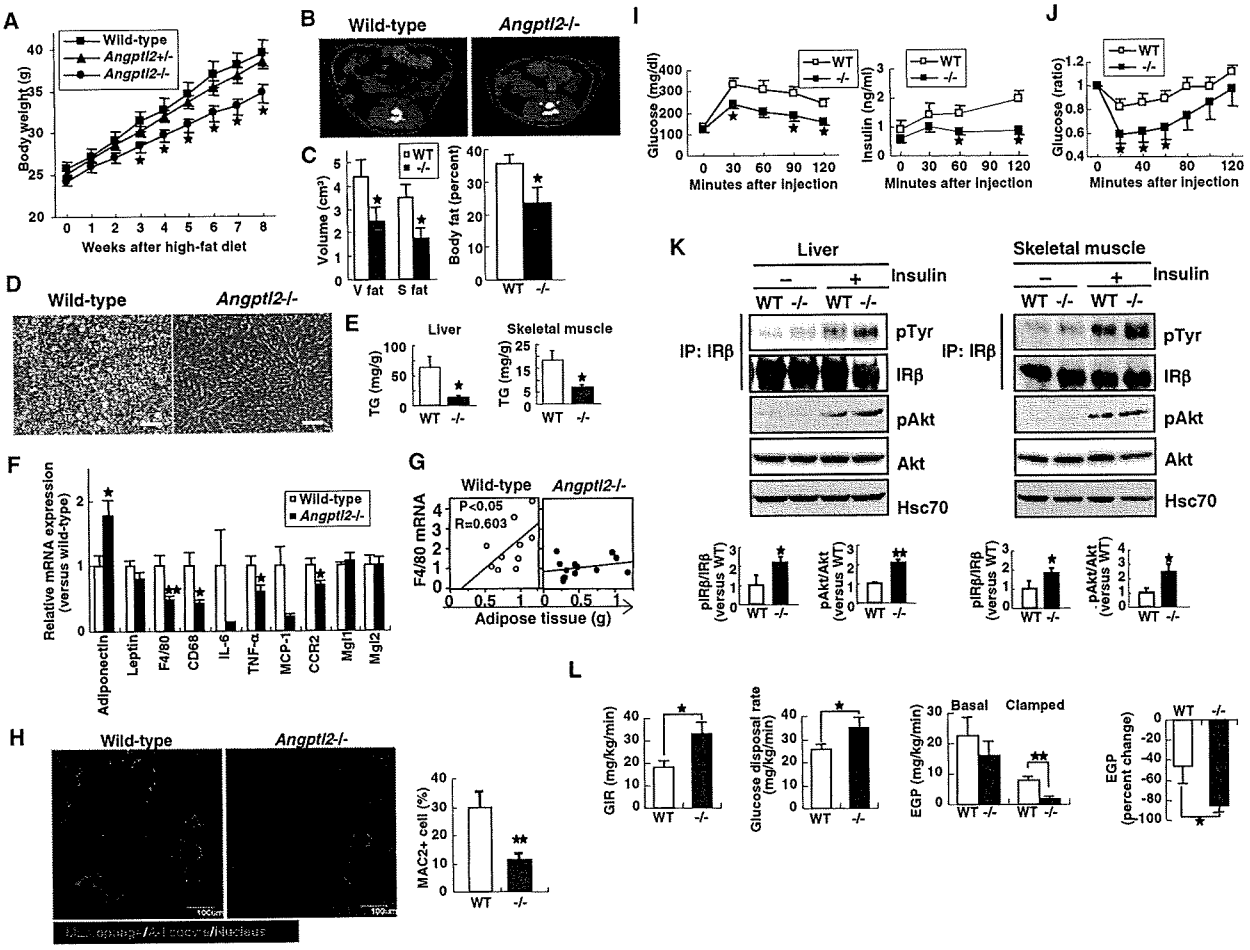

Figure 5. Deletion of Angptl2 Reduces Adipose Tissue Inflammation and Systemic Insulin Resistance in Dietary Obese Mice

Analyses of *Angptl2*$^{-/-}$ and wild-type mice fed a HFD for 8 weeks (A–L).

(A) Body weight of each genotype (n = 8–16 per group) at the indicated times (weeks) after initiation of a HFD.

(B and C) Representative CT findings (B) and quantitative comparison of the visceral (V) and subcutaneous (S) fat volume and total percent body fat (C) in *Angptl2*$^{-/-}$ mice and wild-type mice (n = 5–7 per group).

(D) HE-stained liver sections from *Angptl2*$^{-/-}$ and wild-type mice. Scale bar, 100 μm.

(E) Triglyceride (TG) content of liver and skeletal muscle from *Angptl2*$^{-/-}$ mice and wild-type mice (n = 6 per group).

(F) Quantitative RT-PCR of mRNAs encoding adipocytokines and macrophage markers in epididymal adipose tissue from *Angptl2*$^{-/-}$ and wild-type mice (n = 11–12 per group).

(G) Correlation between F4/80 mRNA expression and epididymal adipose tissue weight in *Angptl2*$^{-/-}$ mice and wild-type mice (n = 11–12 per group). Correlation coefficient (R) and probability (P) values are shown.

(H) Immunohistochemistry of adipose tissue using the macrophage marker MAC2 and adipocyte marker perillipin. Representative photographs and quantitative comparisons of MAC2-positive cells (n = 6 per group) are shown. Scale bar, 100 μm.

(I and J) Glucose (I) and insulin (J) tolerance tests in *Angptl2*$^{-/-}$ mice and wild-type mice (n = 5 and n = 10 per group, respectively).

(K) Insulin signaling in the liver and skeletal muscle of *Angptl2*$^{-/-}$ (KO) and wild-type (WT) mice. Representative western blots and quantitative data for the total and phosphorylated forms of insulin receptor β subunit (IRβ) and Akt are shown (n = 4 per group).

(L) Glucose infusion rate (GIR), glucose disposal rate, endogenous glucose production (EGP) during the basal and clamped states, and percent change in EGP between the states in *Angptl2*$^{-/-}$ (KO) and wild-type (WT) mice (n = 5–7 per group). Data are mean ± SEM, *p < 0.05 and **p < 0.01 compared with controls.

littermates as controls. There was no difference of weight gain between aP2-Angptl2 mice and control wild-type mice fed a normal chow diet (Figure 6A). However, immunohistochemistry using Mac2 revealed accumulation of macrophages in crown-like structures within the adipose tissue of aP2-Angptl2 mice, whereas fewer Mac2-positive cells were observed in wild-type mice (Figure 6B). RT-PCR analysis revealed that inflammatory cytokines (IL-6, TNF-α, and IL-1β) and general (CD68) and inflammatory (CCR2) macrophage markers were increased in the adipose tissue of aP2-Angptl2 mice, while adiponectin and leptin were unchanged (Figure 6C). Lectin staining showed an increase of adherent leukocytes in vessels within the adipose tissue of aP2-Angptl2 mice, while few leukocytes were detected in the vessels of wild-type mice (Figure 6D). There was no

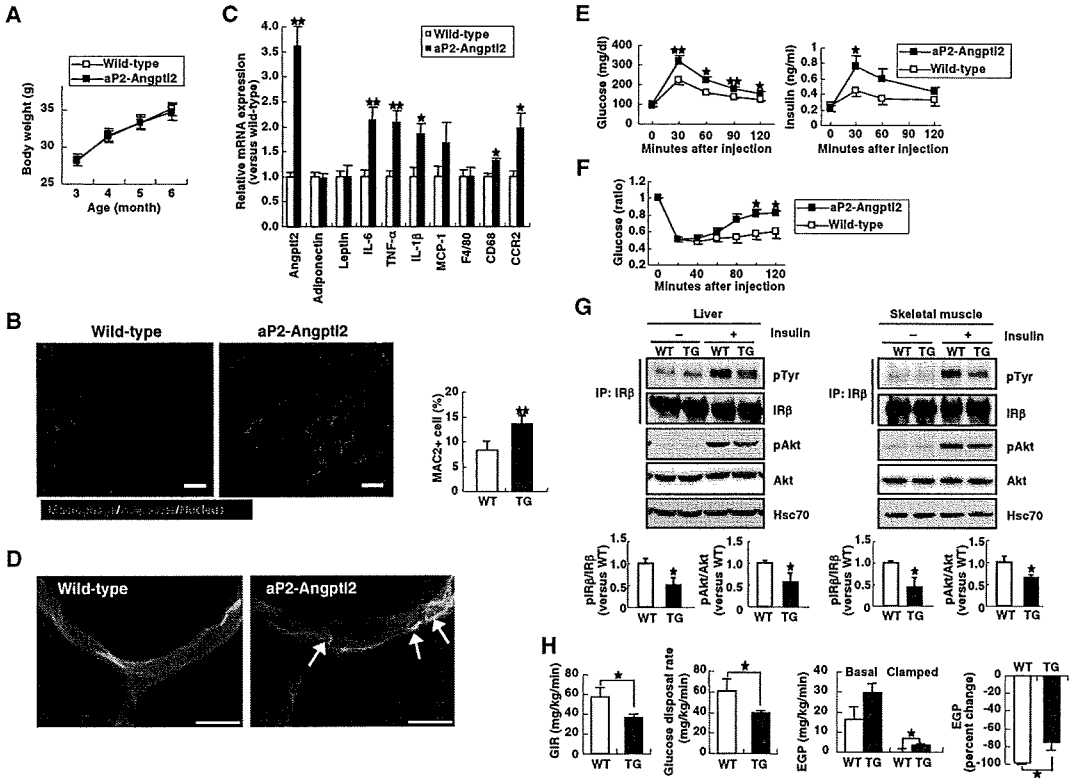

Figure 6. Angptl2 in Adipose Tissue Induces Local Inflammation and Systemic Insulin Resistance

Analyses of aP2-Angptl2 and wild-type mice at 16 weeks of age (B–H).

(A) Body weight of aP2-Angptl2 and wild-type mice (n = 14–16 per group) at the indicated ages (months).

(B) Immunohistochemistry of adipose tissue using the macrophage marker MAC2 and adipocyte marker perillipin. Representative photograghs and quantitative comparison of MAC2-positive cells are shown (n = 6 per group). Scale bar, 50 μm.

(C) Quantitative RT-PCR of mRNAs encoding adipocytokines and macrophage markers in epididymal adipose tissue from aP2-Angptl2 mice and wild-type mice (n = 6 per group).

(D) Blood vessels in epidydimal adipose tissue from aP2-Angptl2 and wild-type mice. Arrows indicate adherent leukocytes on the walls of enlarged vessels in aP2-Angptl2 mice. Scale bar, 25 μm.

(E and F) Glucose (E) and insulin (F) tolerance tests in aP2-Angptl2 mice and wild-type mice (n = 10–12 per group).

(G) Insulin signaling in the liver and skeletal muscle of aP2-Angptl2 (TG) and wild-type (WT) mice. Representative western blots and quantitative data for the total and phosphorylated forms of insulin receptor β subunit (IRβ) and Akt are shown (n = 4 per group).

(H) Glucose infusion rate (GIR), glucose disposal rate, endogenous glucose production (EGP) during the basal and clamped states, and percent change in EGP between the states in aP2-Angptl2 (TG) and wild-type (WT) mice (n = 7 per group). Data are mean ± SEM, *$p < 0.05$ and **$p < 0.01$ compared with controls.

difference of blood vessel density between aP2-Angptl2 mice and control mice (Figure S12C). aP2-Angptl2 mice showed glucose intolerance and insulin resistance in the GTT and ITT, respectively (Figures 6E and 6F). Insulin signaling was diminished in both liver and skeletal muscle of aP2-Angptl2 mice compared with wild-type mice (Figure 6G). The hyperinsulinemic-euglycemic clamp tests also revealed insulin resistance in both skeletal muscle and liver of aP2-Angptl2 mice, since the glucose infusion rate, whole-body glucose disposal rate, and percent change of endogenous glucose production between basal and clamp states were reduced in aP2-Angptl2 mice compared with wild-type mice, while hepatic glucose production during the clamp period was increased in aP2-Angptl2 mice compared with control mice (Figure 6H). These results indicated the presence of insulin resistance in both the skeletal muscle and liver of nonobese aP2-Angptl2 mice.

DISCUSSION

We demonstrated that Angptl2, a member of the Angptl family, is a key mediator of chronic adipose tissue inflammation and obesity-related systemic insulin resistance.

Here we showed that Angptl2 is an adipocyte-derived inflammatory mediator, with increased expression at both the mRNA and protein levels in obesity. Hypoxia and ER stress, which are enhanced in obese adipose tissue (Hosogai et al., 2007; Nishimura et al., 2008; Schenk et al., 2008; Ye, 2009), both increased Angptl2 expression or secretion in adipocytes. Various changes of the microenvironment observed in the adipose tissue of obese animals, such as inflammation and hypoxia, could also promote ER stress (Schenk et al., 2008). Therefore, Angptl2 production by adipocyte should be increased by hypoxia and ER stress in obesity.

It is noteworthy that the circulating Angptl2 level was positively correlated with obesity-related metabolic changes. The difference of circulating Angptl2 protein levels between Angptl2 Tg mice and wild-type mice was only 1.5-fold, but tissue Angptl2 levels showed a 3- to 5-fold difference (data not shown). Therefore, the modest difference of circulating Angptl2 levels in humans may reflect a larger alteration of adipose tissue Angptl2 expression, which could promote inflammation of adipose tissue, resulting in systemic insulin resistance. We also do not exclude the possibility that there is a direct inhibitory effect of circulating Angptl2 on insulin sensitivity in other peripheral tissues, such as skeletal muscle or the liver, because glucose clamp studies and western blotting analysis of insulin signaling revealed that both skeletal muscle and liver were target organs for Angptl2-related insulin resistance in mice. Other Angptl family molecules function in an endocrine manner to regulate lipids, glucose, and energy metabolism (Hato et al., 2008; Oike et al., 2005a, 2005b), so further studies are needed to clarify whether Angptl2 might also act in an endocrine manner.

Angptl2 contains an N-terminal coiled-coil domain and a C-terminal fibrinogen-like domain. The coiled-coil domain is required for oligomerization, which is necessary for its maximum activity, while the fibrinogen-like domain shares high homology with the analogous domain of fibrinogen. Fibrinogen acts as a ligand of the receptors for integrins such as αvβ3, α5β1, and αMβ2 (Herrick et al., 1999; Mosesson, 2005), which are heterodimeric transmembrane glycoproteins that mediate cell-extracellular matrix and cell-cell adhesion (Hynes, 2002). Angptl3 was reported to promote angiogenesis through integrin αvβ3 (Camenisch et al., 2002). In this study, we found that Angptl2 acted on endothelial cells through integrin α5β1 and influenced monocytes/macrophages through integrins α4 or β2. Several reports have indicated that integrin α5β1 signaling activates Rac1 in endothelial cells (Dormond et al., 2001; Mettouchi et al., 2001), in agreement with our finding that Angptl2 promotes Rac1 activation in endothelial cells. We also found that Angptl2 induced the chemotaxis of endothelial cells by in vitro time-lapse imaging analysis and an in vivo mouse cornea neovascularization assay. In contrast, constitutive overexpression of Angptl2 in mouse skin or adipose tissue induced pathological vascular inflammation but did not increase vascularization or ameliorate hypoxia in the adipose tissue of mice with dietary obesity (Figure S12D). The cornea is an avascular tissue and thus is isolated from circulating soluble bioactive mediators, whereas various angiogenesis-related factors exist in highly vascular tissues such as the skin and adipose tissue. Taken together, these findings indicate that Angptl2 may function differently in different tissues, but it promotes vascular inflammation rather than angiogenesis, at least in adipose tissue that develops in obese mice.

Potentially relevant to these findings, we observed that Angptl2 stimulated the nuclear translocation of NF-κB and degradation of IκB in cultured vascular endothelial cells, findings consistent with a previous report that integrin α5β1 signaling activates NF-κB-dependent expression of genes that are important for inflammation (Klein et al., 2002). There have been several other reports that Rac1 activates NF-κB (Perona et al., 1997; Sulciner et al., 1996), which is also consistent with our findings. An important aspect of inflammation is the recruitment of immune cells to affected tissues (Luster et al., 2005). This process requires adhesion of the immune cells to endothelial cells, allowing extravasation into the interstitium, followed by adhesion of immune cells to the extracellular matrix that enables migration toward the site of inflammation. In this regard, Angptl2 not only activated NF-κB in endothelial cells, which could induce expression of adhesion molecules (such as ICAM, VCAM, and selectin) and thus facilitate adhesion of immune cells to endothelial cells, but also promoted the migration of monocytes. Immune cells express integrins α4 or β2, as well as α5β1, which mediate cell adhesion, migration, activation, and production of proinflammatory cytokines through activation of NF-κB (Hynes, 2002; Rose et al., 2007; Roman et al., 2004; Graves and Roman, 1996), suggesting that Angptl2 may activate monocytes via such integrins. It remains to be clarified whether only Angptl2 among the Angptl family shows a stimulatory effect on adipose tissue inflammation, because some other members of this family bind to integrins (Camenisch et al., 2002), and Angptl4 is also abundantly expressed in adipose tissue. The skin tissue of K14-Angptl4 mice showed no inflammatory changes (Ito et al., 2003), unlike that of K14-Angptl2 mice. Moreover, there was no correlation between the serum Angptl4 concentration and Angptl2-related metabolic factors. These findings suggest that the effects of Angptl4 on endothelial cells and/or immune cells are different from those of Angptl2.

In this study, we demonstrated that Angptl2 deletion not only ameliorated inflammation in adipose tissue but also improved systemic insulin resistance in mice with dietary obesity, although it did not completely normalize their insulin sensitivity to the level seen in mice fed a normal chow diet (Figure S11I). The restoration of insulin sensitivity related to Angptl2 deletion may be attributable to the difference of body fat accumulation between the two genotypes. Since adipose tissue volume was not correlated with macrophage infiltration in *Angptl2*$^{-/-}$ mice, some mechanism other than the difference of adiposity may also have contributed to reducing adipose tissue inflammation in *Angptl2*$^{-/-}$ mice. Actually, constitutive Angptl2 overexpression in adipose tissue induced both local inflammation and systemic insulin resistance in nonobese mice. Since adipose tissue inflammation can be a cause of systemic insulin resistance via the secretion of several inflammatory factors (Apovian et al., 2008; Neels and Olefsky, 2006; Schenk et al., 2008), it is suggested that Angptl2 probably influenced systemic insulin sensitivity by exacerbating adipose tissue inflammation (Figure S13).

Although a reduction of adipose tissue inflammation could well be the main reason for improvement of insulin sensitivity in *Angptl2*$^{-/-}$ mice, some other possible mechanisms remain. Adiponectin can potentially increase insulin sensitivity, and the adiponectin level is usually decreased in obesity (Kadowaki and Yamauchi, 2005). However, there was no difference of circulating adiponecin levels between *Angptl2*$^{-/-}$ and control mice (Figure S11H). On the other hand, *Angptl2*$^{-/-}$ mice had a reduced triglyceride content in both skeletal muscle and liver, which could improve insulin sensitivity in these two organs (Schenk et al., 2008).

Angptl2$^{-/-}$ mice showed reduced body fat and tissue triglyceride accumulation when fed a high-fat diet, although there was no obvious difference of daily food intake and energy expenditure estimated from the O_2 consumption rate. Interestingly, the respiratory quotient of *Angptl2*$^{-/-}$ mice was significantly lower